Impact damage assessment in composite laminates using infrared thermography

8

Morteza Moradi[1], *Mathias Kersemans*[2], *Stefano Sfarra*[3] *and Dimitrios Zarouchas*[1]

[1]Center of Excellence in Artificial Intelligence for Structures, Prognostics & Health Management, Aerospace Engineering Faculty, Delft University of Technology, South Holland, Delft, The Netherlands, [2]Mechanics of Materials and Structures (UGent-MMS), Department of Materials, Textiles and Chemical Engineering, Ghent University, East Flanders, Gent, Belgium, [3]Department of Industrial and Information Engineering and Economics (DIIIE), University of L'Aquila, Province of L'Aquila, L'Aquila, Italy

8.1 Introduction

It is well known that the damage to composite structures caused by impact loadings is one of the most critical problems inhibiting the development and the widespread application of such materials. Technically speaking, "impact" is a term in mechanics referring to a high force or shock applied over a short time when two (or more) objects collide that should be refined according to the velocity of the impactor, that is, <10 m/s (low-velocity), between 10 and 50 m/s (intermediate), from 50 to 1000 m/s (high-velocity or ballistic), and between 2 and 5 km/s (hypervelocity) impacts.

Impact damage in composites may be evaluated, detected, studied, and quantified by several techniques; one of these is infrared thermography (IRT) (Maldague, 2001). Some of the precursors in the application of such a technique in composites were Russell and Henneke II, which deepened the problem using both active and passive approaches (Henneke & Russell, 1983) and vibrothermography (VT) (Russell & Henneke, 1984). In the latter, they observed a dependence of the temperature patterns upon the frequency of the mechanical excitation. However, in the field discussed in this chapter, it was in 1987 that IRT affirmed its advantages in the scientific community, as evidenced by a couple of highly cited references in the course of the time (Cielo et al., 1987; Patel et al., 1987). In the same year, there was also the affirmation of "image processing" in the title as well as the study of the bi-dimensional heat transfer equation under the VT modality (Potet et al., 1987). Five years later, Busse et al. demonstrated the effectiveness of "thermal wave thermography" for inspection (Busse et al., 1992). It offers several advantages over the traditional thermal wave and thermography techniques, providing increased

Non-destructive Testing of Impact Damage in Fiber-reinforced Polymer Composites.
DOI: https://doi.org/10.1016/B978-0-443-14120-1.00008-X

depth range, shorter imaging time, depth profiling, and broader application potential. In 1993, the finite element (FE) method based on the 3D theory of linear elasticity was introduced for studying delamination dynamics over a broad frequency range. By utilizing thermographic and thermoelastic nondestructive testing (NDT) techniques, it was found that, at a particular frequency region, local flaw vibration causes the dissipation of mechanical energy into heat (Tenek et al., 1993). Rantala et al. presented an NDT method based on lock-in (stimulated by a modulated heat source) thermography with mechanical heat excitation. The phase information increased the reliability of the defect detection after impact loadings (Rantala et al., 1996). Karger-Kocsis, instead, evaluated the fracture and failure behavior of weft-knitted glass fiber fabric-reinforced polypropylene composite sheets produced by hot pressing; in this case, acoustic emissions (AEs) and IRT were used, the latter intended to detect heat rise in both the wale and course directions of the knit under various loading conditions (Karger-Kocsis & Czigány, 1998). The year 1998 marks another crucial step forward in the application of IRT to impact damage assessment of composite laminates since lock-in thermography was joined with water-coupled ultrasonic excitation (Rantala et al., 1998), and the defects provoked were detected quantitatively (Ball & Almond, 1998). Usamentiaga et al. (2014) and Ciampa et al. (2018) provide comprehensive reviews of IRT as an NDT technology in various domains and active IRT with a focus on aerospace applications, respectively.

It is possible to understand how the use of IRT has been of paramount importance in the evaluation of impacts in composites both during dynamic (Hansen, 1999) and static (Gros et al., 1999) configurations, also combined with additional NDT methods such as ultrasonic C-scans, stimulated shearography, electromagnetic methods, and optical fiber health monitoring systems (Balageas et al., 2000; Bates et al., 2000; Wong et al., 1999). After 2000, there was a growth in research dedicated to studying impact mechanisms in advanced composites, manufactured with hybrid fibers or adhesively bonded. One can refer to the work of Schroeder et al. (2002) to demonstrate the impact of environmental and mechanical exposure on bonded joints, and to Avdelidis et al. (2004) to assess thermal contact resistance between surfaces. Additionally, Meola et al. (2006) can be cited to emphasize the contribution of lock-in thermography and Bhatt et al. (2008) to investigate the degree of substrate damage caused by increasing projectile velocity. In this trend, it is of interest to highlight the work of Takeda et al. (2007), which integrated fiber Bragg grating with NDT methods (among which IRT) for the monitoring of impact damages and fatigue tests of composite wing structures.

At the end of 2009, new ideas concerning the evaluation of damage shape at the post-impact stage were brought to light by De Rosa et al., who focused the attention on glass/jute hybrid laminates inspected by AE and IRT (De Rosa et al., 2009) and on E-glass/basalt woven fabric interply hybrid laminates subsequently (De Rosa, 2011). Thanks to IRT, some researchers were able to conduct a more detailed study of the impact phenomenon on composite laminates. Meola and Carlomagno (Meola & Carlomagno, 2010) employed IRT in two ways to assess the influence of low-velocity impacts on glass fiber-reinforced polymer (GFRP) materials: on-line monitoring and lock-in-based inspection. On-line IRT monitoring revealed that the

thermoelastic effects induce a momentary (fraction of a second) cooling, followed by the dissipation of impact mechanical energy, which causes matrix microcracks, delamination, and fiber breakages, and a subsequent heating up. When the lock-in IRT is compared to the on-line IRT, the warmer area monitored in the on-line IRT represents the extension of the damaged zone.

One of the pros of IRT is, for sure, its portability. Although measurements had been conducted prior to the early 2010s, the work of Garnier et al. (2011) was a precursor to in-situ investigations, as it focused on evaluating barely visible impact damage (BVID)—a concept that has been repeatedly emphasized by other research groups (Herb et al., 2012; Montanini & Freni, 2012; Suzuki et al., 2012). The 2013 year marks a turning point in the automatic characterization of impact damage in carbon fiber-reinforced polymers (CFRPs) by IRT, thanks to the work of Usamentiaga et al., which also deepened the feature extraction and analysis problem. Although the title seems simplistic, it is essential to remark that tests were carried out over related specimens containing impact damage of different energies, showing acceptable performance for the classifier (Usamentiaga et al., 2013b). Regarding portability, the possibility of integrating IRT with an unmanned aerial vehicle (UAV) attracted researchers' interest. For instance, Moran and Rajic (Moran & Rajic, 2019) evaluate the remote line scan thermography (LST) aimed at the viability of UAV applications to monitor BVID in composites. After optimizing the experimental setup by exploiting the numerical simulation and a light-weight luminaire, they developed an innovative type of scanning pulse phase thermography known as dynamic pulse phase thermography (DPPT). The processing algorithm of DPPT has been designed to account for the restriction of not having access to the entire thermal data sequence until the end of the scan, facilitating real-time inspection.

Considering the object's 3D shape is another remarkable and advantageous aspect of an NDT inspection, particularly for composite structures that may be made in a curved shape. Active 3D thermography (A3DT) combines active thermography with the 3D shape of the object being inspected. Initial studies of A3DT techniques relied on at least two separate IR sensors (Hellstein & Szwedo, 2016). The pertinent algorithms, which are referred to as feature-based registration models (Chen et al., 2019), register images based on keypoint tracking and matching. Given the disadvantage of having to combine the two mathematical models of 3D reconstruction and IR inspection in the case of two cameras and two excitations, Deng et al. (Deng et al., 2022) established a feature-free registration model to utilize just one IR camera and one laser for A3DT inspection of nonplanar GFRP and CFRP.

Last but not least, many researchers have greatly centralized their efforts above all in studying the best machine or deep learning algorithms of artificial intelligence (AI), for example, to be applied in detecting BVID in composite laminates (Alhammad et al., 2022; Deng et al., 2023). For instance, Ruan et al. (2020) adjusted a generative adversarial network architecture for high-resolution IRT defect detection on both regularly and irregularly shaped CFRP specimens containing inner debond defects. Promising outcomes have been achieved where the effectiveness of the suggested approach can achieve end-to-end defect detection when compared to state-of-the-art deep semantic segmentation algorithms. The data from

various optical pulsed thermography (OPT) systems and the data from various shapes demonstrate the algorithm's reliability. Liu et al. (2023) proposed an unsupervised deep autoencoder thermography (DAT) method to improve the accuracy and reliability of defect detection in CFRP specimens with multiple defects at different depths and locations. By displaying the hidden-layer features of the deep learning network, the DAT model's functionality for feature extraction, image smoothing, and denoising was investigated. Experimental findings indicated that the DAT model was superior to the earlier IRT data processing methods based on dimensionality reduction in terms of accuracy and reliability of defect detection. In active IRT, the tendency is to inspect swiftly, accurately, and intelligently by introducing multiple-mode stimulation sources and AI, according to the reference (He et al., 2021), which reviews how deep learning has been applied to IRT. With the rapid advancement of deep learning, IRT's applications are greatly expanding and becoming more intelligent and automated.

It is on the above-mentioned key points that the present chapter will take shape; in particular, active IRT methodologies based on excitation sources (Section 8.2), heating waveforms and data processing (Section 8.3), case studies, and related discussions (Sections 8.4 and 8.5) will be accurately deepened by the authors to the benefit of the readers.

8.2 Infrared thermography inspection apparatus and device specifications

The use of thermography has grown significantly in recent years, especially since IRT is now widely used to inspect different composite components. The appropriate use of complex IR systems and equipment is critical to the effectiveness of infrared thermal inspections. For the proper selection and operation of IRT inspection equipment, professionals in the field of NDT of composite structures can rely on internationally recognized standards.

The performance of IRT in the context of impact damage detection is affected by several key features of the IR cameras that are employed. In order to attain accurate and reliable results, several specifications, such as thermal sensitivity (noise equivalent temperature difference, NETD), spatial resolution, and dynamic range, should be considered.

Regarding IRT, there are various helpful standards:

- **ISO 18434-2 (2019):** "Condition monitoring and diagnostics of machine systems—Thermography—Part 2: Image Interpretation and diagnostics."
- **ASTM E1311-14 (2022):** "Standard Practice for Minimum Detectable Temperature Difference for Thermal Imaging Systems"
- **ASTM E1862-14 (2022):** "Standard Practice for Measuring and Compensating for Reflected Temperature Using Infrared Imaging Radiometers"
- **ASTM E1933-14 (2022):** "Standard Practice for Measuring and Compensating for Emissivity Using Infrared Imaging Radiometers"

It is important to note that the characteristics may vary based on the specific requirements of the inspection scenario, the size and nature of the composite structures, and the type of impact damage being targeted, such as BVID. Additionally, advancements in technology may result in improvements beyond the baseline recommendations. When selecting an IR camera for impact damage detection in composite structures, it is advisable to consult with manufacturers' specifications and technical documentation, as they often provide detailed information on thermal sensitivity, spatial resolution, and dynamic range specific to their products. Key characteristics of IRT systems that have been employed in some studies for impact detection in composite materials are listed in Table 8.1. The reader is also referred to ASTM E2582 for "Standard Practice for Infrared Flash Thermography of Composite Panels and Repair Patches Used in Aerospace Applications."

8.3 Active infrared thermography methodologies based on the excitation source

NDT using IRT can be done in two ways: passive and active. The active approach is more commonly used, where an external stimulus is applied to the material during the inspection. The stimulation generates heat, which diffuses through the specimen as thermal waves either from the surface to the subsurface or as a result of volumetric heating. When the thermal waves reach an anomaly or damage, their diffusion rate is changed, resulting in a thermal contrast on the surface above the defect. Various stimulation methods can be used, such as optical (e.g., halogen heat lamps and lasers) (Bayat et al., 2019; Moradi & Safizadeh, 2019a), mechanical (e.g., ultrasonic waves and vibrations) (Hedayatrasa et al., 2021), or inductive (i.e., induced eddy currents and microwaves) (Usamentiaga et al., 2014). These excitation methods have been introduced to cope with the limitations of methods such as thermal blankets and heat guns, which are the most basic excitation techniques initially used for IRT inspections, and to enhance defect detection performance. This section provides a summary of IRT methods categorized based on the thermal excitation sources: optically stimulated thermography (OST), mechanically stimulated thermography (MST), and inductively stimulated thermography (IST).

8.3.1 Optically stimulated thermography

The most common excitation methods are the optical techniques (OST) (Busse et al., 1992; Maldague & Marinetti, 1996; Moradi & Safizadeh, 2019c), which use halogen lamps for both continuous and modulated heating as well as flash lamps, which emit energy pulses. By adjusting the number of lamps, analyzing both the heating and cooling phases, and offering a high repeatability rate, both technologies are suitable to stimulate large or small regions. The most popular OST methods for aerospace applications, based on the sort of external optical source used to generate thermal waves, step heating thermography (SHT), long pulse thermography (LPT),

Table 8.1 Key parameters of infrared thermography systems used in research for impact detection in composite materials.

Damage & material	Thermal resolution[a] (mK)	Imaging resolution[b] (pixel)	Temporal resolution[c] (fps - Hz)	Wavelength (μm)	Heating	References
FBH in PMMA	70	320 × 240	3.75	7.5−13	PIT—2 × Xe flash lamps (2000 J/F for 3 ms)	Ishikawa et al. (2013)
BVID in CFRP	30	320 × 256	150	3−5	LIT	Fierro et al. (2017)
BVID in CFRP	–	640 × 512	50	–	PIT—2 × capacitor banks-powered Xenon flash lamps (2 kJ)	Deng et al. (2023)
BVID in CFRP	–	512 × 512	50 and 85	3−5	PIT—Photographic/Power flashes	Alhammad et al. (2022)
BVID in CFRP	20	320 × 256	383	1.5−5	ECPT—Easyheat 224 from Cheltenham induction heater (2.4 kW)	He et al. (2014)
FBH and BVID in CFRP	50 50 18	320 × 256 640 × 480 640 × 512	60 50 100	7.5−13 7.5−14 3.0−5.0	LST—Remote line scan thermography	Moran and Rajic (2019)
FBH and BVID in woven fabric composites (CETEX and CFRP)	<20	640 × 512	30	3−5	PIT—Hensel linear flash lamp (6 kJ for 5 ms)	Poelman et al. (2023)
Impact in CFRP	20	320 × 256	50	2.5−5.1	SHT—3 × halogen lamps at 80% capacity (1 kW for 15 s)	Usamentiaga et al. (2013a)

[a]Thermal resolution, measured as noise equivalent temperature difference (NETD), signifies a device's sensitivity, or its ability to detect minimal temperature differences. It is a ratio of the object's signal to the background's signal, accounting for the thermal sensor's noise.
[b]Imaging resolution is the image contrast and is directly related to the number of pixels a thermal imaging camera has.
[c]Temporal resolution or frame rate provides information on the time difference between the acquisitions of two images over the same area. The values in the table are those that have been set and reported in the references; this could be adjusted depending on the infrared camera.

optical pulsed thermography (OPT), lock-in thermography (LIT), frequency modulated thermography (FMT), laser-spot thermography (LST), and laser-line thermography (LLT) (Ciampa et al., 2018).

Plenty of research has been conducted to assess OST's capacity for delamination detection, which is one of the critical and main damages caused by impact in composite structures. To evaluate the diffusivities for the intact and defective regions, OPT is utilized in both transmission and reflection modes (Maierhofer et al., 2014), providing satisfactory outcomes for damage identification. While the transmission setup could detect deeper artificial delaminations, the maximum detectable depth in the reflection setup was limited to 1.7 mm. Conversely, the reflection setup outperformed the transmission setup in identifying shallow delaminations. Nevertheless, the effectiveness of the IRT method depends on the thermal resistance between the host (polymeric) material and the defect, and as a result, an appropriate method to simulate a genuine delamination defect from the perspective of IRT is essential in order to accurately demonstrate the true performance and limitations of this NDT method (Moradi & Safizadeh, 2019b). Another study on the subject of delamination detection is (Usamentiaga et al., 2013a), which suggests a methodology for automatically detecting impact damage in CFRP by utilizing a neural network to process thermograms recorded by an active IRT setup. The pulsed phase thermography algorithm was applied for the SHT technique, and the collected data was then processed. Examinations were performed on a number of specimens with similar material types but various features and synthetic damage introduced by impacts with energies ranging from 6 to 50 J. The accurate detection of every defect shows that the suggested method is reliable and effective under various conditions. In the case of woven fabric-reinforced polymers, the OST faces more challenges in achieving reliable damage detection due to the intense perturbations and patterns in the background of the thermograms caused by the weave fabric of the composite. In this regard, the data processing algorithms could be adapted to the material's fabric. For example, Poelman et al. (Poelman et al., 2023) developed k-space filtering, a processing algorithm based on the discrete 2D Fourier transform, to automatically decompose a thermographic image into an image containing the organized thermal background attributed to the woven fabric and a remaining image reflecting other characteristics, such as defects.

Techniques used for OST generally yield satisfactory outcomes. Nevertheless, some particular defects are challenging to identify by OST methods because they provide insufficient thermal contrast, such as some imperfections and inserts in composite materials, especially the ones perpendicular to the surface under inspection. Advanced stimulation methods, such as MST and IST, were established to get around these restrictions.

8.3.2 Mechanically stimulated thermography

The main inspiration for MST, also called VT, came from mechanical vibration-based stimulations. VT (Favro et al., 2000; Henneke et al., 1979; Holland et al., 2011; Russell & Henneke, 1984; Tenek et al., 1993), also referred to as (ultra)sonic

(infrared) thermography (Mendioroz et al., 2017; Solodov et al., 2015b; Tsoi & Rajic, 2011; Umar et al., 2017) or thermosonics (Dyrwal et al., 2018; Solodov et al., 2015a), is an active IRT technique that relies on vibration-induced heating phenomena to detect internal defects. Mechanical vibrations are typically induced by a piezoelectric actuator that is bonded to the surface of the test specimen. The increased strain energy density around defects, in combination with the normal and tangential interaction of the defect's interfaces, leads to the dissipation of vibrational energy, resulting in localized volumetric heating. Depending on the orientation, asperities, tightness, and stress state of the defect, various dissipation mechanisms may take place, such as friction, adhesion hysteresis, viscoelastic damping, thermoelastic damping, and even plastic deformation at the crack tips (Holland et al., 2011; Renshaw, 2009; Renshaw et al., 2011; Truyaert et al., 2019). The vibration-induced heat near the defect diffuses to the surface of the test component, where it is monitored with a sensitive infrared camera. One of the main benefits of VT is its ability to detect defect types that are hard to identify by other (thermographic) NDT techniques, for example, kissing bonds or defects oriented normal to the inspection surface (Mendioroz et al., 2019).

In classical VT, a high-power (ultra)sonic horn of a few kilowatts is used in order to provide a short, yet intense, vibrational stimulation to the test specimen (Favro et al., 2000; Holland et al., 2011). The (ultra)sonic horn vibrates at its resonant frequency (typically in the range of 10−30 kHz) and applies a broadband hammer-like load to the object under inspection. Although acceptable vibrothermal results have been achieved for a variety of materials and defect types, there are some practical challenges. The use of high-power ultrasonic horns requires a power amplifier and a clamping device, making the setup more complex. Additionally, for polymer-based materials, the strong vibrational stimulus may induce thermal degradation near the excitation location (Caruso et al., 2009).

Low-power resonant VT, on the other hand, tunes the vibrational excitation frequency to either a global resonance of the test piece or a local defect resonance (LDR). In the first case, an electrodynamic shaker is typically used to resonate the test piece at a specific modal frequency or a combination of modal frequencies (normally less than 1000 Hz). This approach, which is also called self-heating-based VT (Katunin, 2018), boosts the global heating of the specimen due to vibrational damping phenomena and yields distinct thermal gradients near defective areas. VT utilizing the concept of LDR became popular in the last decade, but it was already introduced in the 1980s in a set of related studies (Russell & Henneke, 1984; Tenek et al., 1993). Nowadays, researchers employ low-power piezoelectric actuators or contactless air-coupled ultrasound transducers to excite the test piece at an LDR frequency (typically $>$20 kHz) and to selectively stimulate resonance modes of damage features. This local resonation leads to a significant increase in the vibration-induced heating at the targeted defect (Dionysopoulos et al., 2018; Fierro et al., 2017; Solodov et al., 2015b; Solodov & Busse, 2013). Both out-of-plane and in-plane LDR can be employed, with the latter being shown to have higher heating efficiency due to its elevated operating frequency as well as the dominant lateral rubbing of the defect's interfaces (Segers et al., 2019). The high-frequency vibrational signal is often

amplitude-modulated at a low frequency in order to match the thermal diffusion length of the vibration-induced heating with the defect depth. Subsequent lock-in analysis then results in so-called lock-in VT, which has an increased signal contrast and sensitivity, especially for the phase image (Tenek et al., 1993). Nevertheless, there is a fundamental issue with low-power VT based on LDR: how to know the LDR frequency without prior information on damage characteristics? To cope with this, recent work has introduced the use of broadband vibrational excitation signals, for example, sweep sine, which may stimulate unknown LDRs within the bandwidth of excitation (Hedayatrasa et al., 2021; Hedayatrasa et al., 2020; Rahammer & Kreutzbruck, 2017; Segers et al., 2019). In particular, a repetitive sweep signal was employed in Rahammer and Kreutzbruck (2017), followed by spectroscopic vibrothermal analysis for detecting delaminations in CFRP laminates. If the bandwidth of the sweep signal is sufficiently wide, in-plane LDRs may be triggered, enabling the detection of BVID in CFRPs, even through live monitoring of the surface temperature. When coupled with time-derivative analysis, the imaging quality of damage significantly improves, giving clear indications of delamination fragments in the BVID area (Segers et al., 2019). To correct for the time delay of the vibration-induced heating to reach the inspection surface, two consecutive sweep sines can be employed, one with an up-going frequency rate and the other with a down-going frequency rate. The spectroscopic correlation of the two response signals allows compensation for any thermal delays, and as such, enables the identification of the true LDR frequencies at which vibrothermal images with optimal contrast can be obtained (Hedayatrasa et al., 2020).

8.3.3 Inductively stimulated thermography

Thermo-induction thermography, inductively stimulated thermography (IST), or eddy current-stimulated thermography (ECST) induces eddy currents inside the specimen being inspected by circulating a current along an induction coil at specific frequencies. The bulk is heated by Joule heating, which is caused by different current densities in the areas with imperfections (Usamentiaga et al., 2014). Eddy current IRT was used in He et al. (2014) to investigate the damage in CFRP laminates impacted by different energies from 4 to 12 J. Eddy current IRT offers a higher inspection speed and depth with a better resolution because it incorporates the benefits of traditional eddy current and IRT techniques and is compatible with both reflection and transmission setups. This method, unlike OST, is independent of some surface properties (such as reflectivity) and, like MST, does not need a couplant.

The most common method of stimulation among IST methods is an eddy current pulse with a high-frequency electromagnetic wave, typically with a central frequency of 150−450 kHz (also known as "pulsed ECST"). The excitation duration can vary from a few milliseconds for highly electrically conductive materials (such as metallic materials) up to a few seconds for materials with lower conductivity (e.g., CFRP laminates). Due to the way that it operates, unlike OST, pulsed ECST enables the delivery of heat to penetrate up to a particular depth and is not restricted to some surface properties of the specimen. The skin effect governs the

permeability of magnetic flux in a specimen for a uniformly distributed field excitation that is parallel to the surface (Ciampa et al., 2018).

A single layer of unidirectional CFRP usually has an electrical conductivity of 5 Ms/m in the longitudinal direction and 1 kS/m in the transverse direction (Yang & He, 2015). Inductors employed to inspect composite materials by the ECST method also work properly at high excitation frequencies. As a result, the penetration depth for CFRP with no magnetic penetration is considerably high (50 mm for 100 kHz excitation). Since electrically conductive carbon fibers are incorporated into an insulating resin matrix, this substance has complicated electromagnetic properties. Because electrical and thermal conductivity is maximum along the fiber orientation, recent developments in ECST consist of the detection of hidden defects in the resin (matrix) which is the dielectric part of composite laminates, such as water ingress, material aging, porosity, and delamination (Ciampa et al., 2018).

Yang and He used the ECST method to investigate damages caused by impacts between 2 and 12 J in six CFRP specimens. Their findings demonstrate that the ECST, with a proper processing (filtering) algorithm, has the potential to characterize fibers' structure as well as to inspect surface matrix cracks and delaminations (Yang & He, 2016). Other researchers also employed the ECST to inspect the impacted CFRP laminates, and they processed the thermograms using the popular principal component thermography (PCT) algorithm (He et al., 2014; Liang et al., 2016). The thermograms obtained by the ECST method could be transformed from time to frequency domain, aiming at higher detection performance of delamination in composite laminates thanks to phase images (He & Yang, 2015). Regarding the NDT of damages in impacted CFRPs, a scanning ECST method with a moving induction coil (with a speed of approximately 40 mm/s) over the specimen was also introduced by Thomas and Balasubramaniam (Thomas & Balasubramaniam, 2015). In comparison with a standard ultrasonic C-Scan, the ECST method was able to properly determine the damage location and severity.

8.4 Heating waveforms and data processing

In addition to having different methodologies based on the type of excitation source in active IRT, various heating functions may be employed to excite the object under inspection, specifically for OST, aiming to improve damage detectability and depth resolvability. The waveforms (heat flux) can be in different forms of step or long pulse (SHT or LPT), pulse (PT), sinusoidal (LIT), and modulated waves. In the case of the latter [so-called thermal wave radar (TWR)], a waveform can be modulated in terms of amplitude, frequency, phase, or angle which comprises a combination of both frequency and phase (FPM). It should be noted that LIT is a specific state of AM; however, it will be presented separately to better discuss the relevant concepts and due to the longer history of LIT in IRT. Fig. 8.1 shows the waveforms of step (long pulse), pulse (short pulse or flash), sinusoidal, amplitude modulation (AM), frequency/phase modulation (FM/PM), and angle modulation (frequency-phase modulation, FPM).

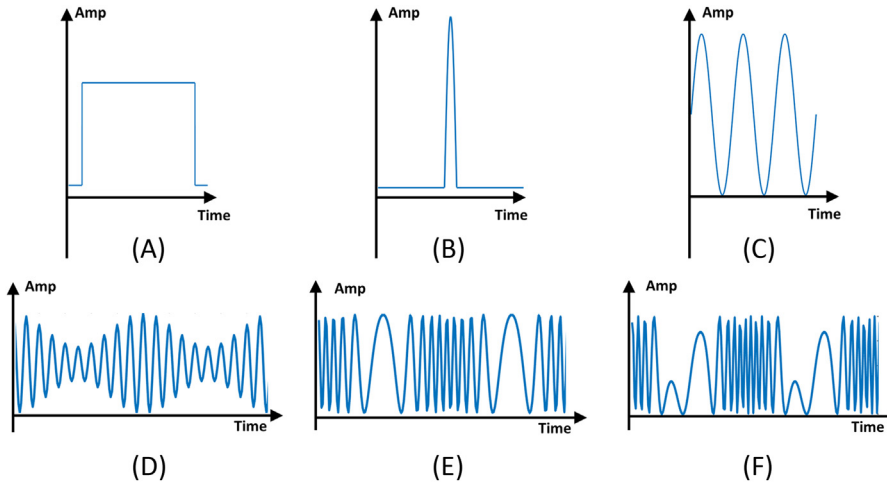

Figure 8.1 Different waveforms including (A) step (for SHT or LPT), (B) pulse (for PT or flash thermography), (C) sinusoidal (LIT), which is a specific type of AM, (D) AM, (E) FM or PM, and (F) FPM (a combination of both FM and PM).

Eq. (8.1) shows a sinusoidal (carrier) wave, which is generally modulated with the information signal ($S_{(t)}$) using analog modulation:

$$C_{(t)} = A_{(t)}\cos(\omega t + \varphi_{(t)}) = A_{(t)}\cos(2\pi ft + \varphi_{(t)}) \tag{8.1}$$

where the amplitude $A_{(t)}$ of the wave varies over time, and the angular frequency of the cosine term is represented by ω. The instantaneous phase deviation is given by $\varphi_{(t)}$. This equation can be used for both AM (where the angle term is constant) and angle modulation (where the amplitude term is constant). Angle modulation (FPM) consists of FM and PM where FM changes the carrier frequency and PM controls its phase deviation. However, both PM and FM are usually performed by the instantaneous phase deviation $\varphi_{(t)}$ (PM by $\varphi_{(t)} = k_p \times S_{(t)}$ and FM by $\varphi_{(t)} = 2\pi k_f \int S_{(t)}dt$). Although angle modulation provides better resistance to noise and interference, it requires more bandwidth. The modulating signal may be analog or digital, with digital signals using the so-called keying technique instead of modulation. Frequency-shift keying (FSK), a form of FM where the carrier's instantaneous frequency is varied across a range of frequencies, is a technique for encoding and transmitting digital data. The fact that FM disregards interference from other frequencies more effectively than an equal-power AM signal owing to its higher signal-to-noise ratio (SNR) is a benefit. The two complementary primary methods of angle modulation, FM and PM, commonly operate in conjunction with one another, which has emerged in IRT under the name "FPM".

All the above-mentioned waveforms can be used for different excitation source-based methods of OST, MST, or IST, among which sinusoidal (LIT method) and pulsed (OPT method) are the two primary methods used in OST. In this section,

according to the type of waveform, the relevant thermal response equations are presented in three subsections: step and pulse waveforms, sinusoidal amplitude modulation, and frequency-phase modulation. The first subsection focuses on step and pulse excitation waveforms, where detailed analytical equations are derived to help understand the heat transform for defected composite materials. Additionally, this subsection provides relevant postprocessing algorithms for thermograms, considering that the choice of the waveform may determine the appropriate postprocessing method. The remaining two subsections are summarized briefly to maintain the flow of the chapter. However, to provide interested readers with further information, relevant sources pertaining to those subsections are introduced.

8.4.1 Step and pulse waveforms

In order to capture the surface's temperature evolution throughout the post-flash cooling phase, pulsed thermography (PT) subjects the object to a short pulse lasting only a few milliseconds (Fig. 8.1B). Despite this, the short pulse time renders it ineffectively responsive to deep flaws with insufficient low-frequency responses and highly sensitive to shallow flaws via enhanced high-frequency responses (Hedayatrasa et al., 2019). The corresponding 1D inhomogeneous heat equation can be solved, resulting in the transient thermal field $T(z,t)$ in PT:

$$\frac{\partial^2 T(z,t)}{\partial z^2} + \frac{g(z,t)}{k} = \frac{1}{\alpha}\frac{\partial T(z,t)}{\partial t};\ t>0 \tag{8.2}$$

where k is the thermal conductivity (W/mK) and $\alpha = k/\rho C$ is the thermal diffusivity (m^2/s) (with ρ the density (kg/m^3) and C the specific heat (J/kg K)). $g(z,t)$ is the heat source, which is $g(z,t) = Q_0\delta(z-z_0)\delta(t-t_0)$ for the case of ideal PT, having an external impulsive heat source located at $z_0 = 0$ and excited at time $t_0 = 0$, with Q_0 the source intensity per unit length (Jm^{-1}). $\delta(z-z_0)$ and $\delta(t-t_0)$ are Dirac's delta functions in space and time, respectively. According to Green's theorem, the solution of the inhomogeneous heat Eq. (8.2) can be expressed as follows (Almond & Pickering, 2012):

$$T(z,t) = \frac{Q_0}{e\sqrt{\pi t}} e^{-\frac{z^2}{4\alpha t}} \tag{8.3}$$

where $e = \sqrt{k\rho C}$ is the thermal effusivity ($Ws^{1/2}m^{-2}K^{-1}$) or thermal inertia of the material, which is an indicator of its capacity to exchange thermal energy with its surroundings (Vavilov & Burleigh, 2020). An increase in temperature at a depth z below the surface at a time t following an even pulse of energy (heat flux) Q_0 is demonstrated in Eq. (8.3). By assuming $z = 0$, it is easy to derive the surface temperature response via Eq. (8.4):

$$T(0,t) = \frac{Q_0}{e\sqrt{\pi t}} \tag{8.4}$$

Eq. (8.4) indicates the thermal response, at the surface ($z = 0$), of a semiinfinite half solid without defect. On the other hand, this equation can be expressed as

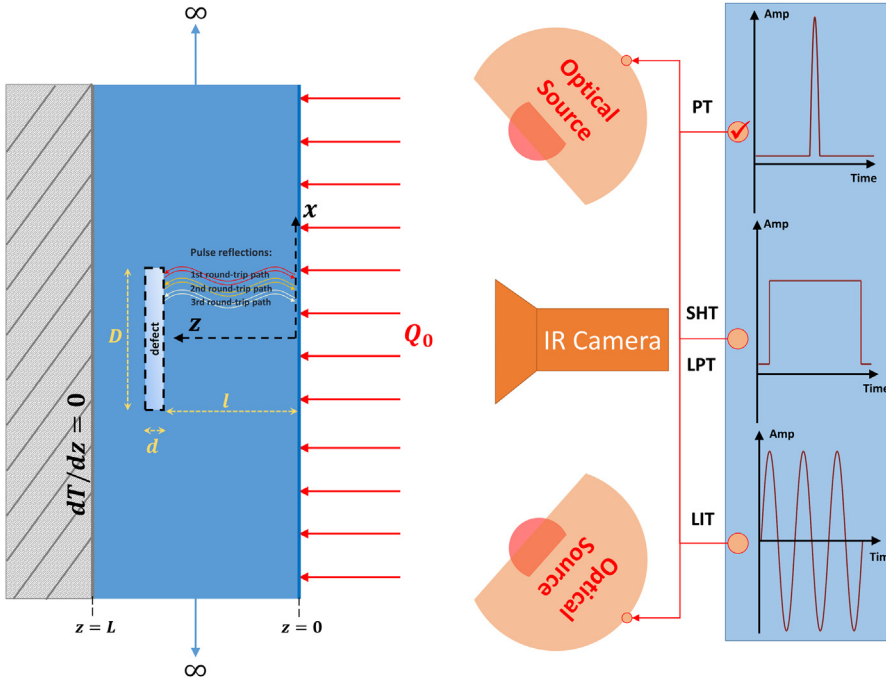

Figure 8.2 The outline of active IRT for an object having a defect.

follows in order to also include a defect at a depth of $z = l$ (see Fig. 8.2):

$$T_d(0,t) = \frac{Q_0}{e\sqrt{\pi t}}\left\{\underbrace{1}_{\text{Sound}} + \underbrace{2\sum_{n=1}^{\infty} R^n e^{-\frac{(nl)^2}{\alpha t}}}_{\text{Defective (contrast)}}\right\};\ T_C(t) = \frac{2Q_0}{e\sqrt{\pi t}}\left\{\sum_{n=1}^{\infty} R^n e^{-\frac{(nl)^2}{\alpha t}}\right\} \tag{8.5}$$

where R is the solid−air interface's effective thermal reflection coefficient, which is approximately 1 (Almond & Pickering, 2012). The first term in the bracket denotes the thermal response at the surface corresponding to the sound region, and the second term denotes that for the defective region, which is also called thermal contrast ($T_C(t)$). Eq. (8.5) can be rewritten by

$$T_d(0,t) = \frac{Q_0}{e\sqrt{\pi t}}\left\{\underbrace{1}_{\text{sound}} + 2\left(\underbrace{Re^{-\frac{(1\times 2l)^2}{4\alpha t}}}_{\substack{\text{1st round}-\text{trip}\\ \text{pulsereflection}}} + \underbrace{R^2 e^{-\frac{(2\times 2l)^2}{4\alpha t}}}_{\substack{\text{2nd round}-\text{trip}\\ \text{pulsereflection}}} + \underbrace{R^3 e^{-\frac{(3\times 2l)^2}{4\alpha t}}}_{\substack{\text{3rd round}-\text{trip}\\ \text{pulsereflection}}} + \ldots\right)\right\} \tag{8.6}$$

where the consecutive terms represent the first, second, third, etc. pulse reflections from the interface of the defect with a thermal reflection coefficient R with respect to the host material, with round-trip paths that are, respectively, $1 \times 2l$, $2 \times 2l$, $3 \times 2l$, etc. The first three round-trip paths of reflection are shown in Fig. 8.2. Eqs. (8.5) and (8.6) do not take into account the lateral diffusion of heat from the defect center to its edge, which is valid when defects have a very large lateral extent ($D \gg l$ for the circular defect of diameter D), and therefore the lateral diffusion consequences to the defect borders are insignificant. To address this physical phenomenon, Eq. (8.5) can be modified according to the underlying assumption that the rate of lateral heat diffusion from the center to the edge of the defect is what constrains the evolution of the thermal contrast across the defect center (Almond & Pickering, 2012):

$$T_d(0,t) = \frac{Q_0}{e\sqrt{\pi t}} \left\{ \underbrace{1}_{\text{Sound}} + \underbrace{\left[2\sum_{n=1}^{\infty} R^n e^{-\frac{(nl)^2}{\alpha t}} \right] \left(1 - e^{-\frac{\left(\frac{D}{2}\right)^2}{4\alpha t}} \right)}_{\text{Defective}} \right\} \tag{8.7}$$

where the curved parentheses of the defective term are a decay factor due to the lateral diffusion. To generalize Eq. (8.7) for multilayer materials (e.g., GFRP or CFRP), which is the focus of the current chapter, an anisotropy factor $m = \alpha_x/\alpha_z$, which indicates the ratio of in-plane to through-thickness thermal diffusivity, is adopted (Almond & Pickering, 2012):

$$T_d(0,t) = \frac{Q_0}{e\sqrt{\pi t}} \left\{ 1 + \left[2\sum_{n=1}^{\infty} R^n e^{-\frac{(nl)^2}{\alpha t}} \right] \left(1 - e^{-\frac{\left(\frac{D}{2}\right)^2}{4m\alpha t}} \right) \right\} \tag{8.8}$$

The defect is presumed to be buried in an object with a thickness that is significantly larger than the defect depth in the basic analytical equations mentioned above. In such a solid, it can be stated that thickness has minimal effect on the thermal decay of the surface over the sound region. However, this thermal deterioration is impacted, and its modification is significant for thinner solids. In order to address this, the contrast (defective) term is reconstructed as the deviation with respect to a sound region of a given thickness L(Almond et al., 2017). Eq. (8.8) can be revised in this regard as follows:

$$T_d(0,t) = \frac{Q_0}{e\sqrt{\pi t}} \left\{ 1 + \left[2\sum_{n=1}^{\infty} R^n \left(e^{-\frac{(nl)^2}{\alpha t}} - e^{-\frac{(nL)^2}{\alpha t}} \right) \right] \left(1 - e^{-\frac{\left(\frac{D}{2}\right)^2}{4m\alpha t}} \right) \right\} \tag{8.9}$$

Although PT is the most popular heating technique, it might not be appropriate for thick composite laminates. Due to the low conductivity of composites, thick structures might require high-intensity pulses. On the other hand, to prevent destroying the structure, pulses must be kept to low levels. With this in mind, SHT or LPT uses a prolonged pulse of low-intensity heat stimuli (a few seconds) (Fig. 8.1A). A number

of the drawbacks of pulse heating for thick composite laminates may be mitigated through these techniques. In contrast to SHT, in which the heating stage is examined, the cooling stage is investigated and postprocessed in LPT, similar to PT (Hedayatrasa et al., 2019). By integrating the impulse response using Eq. (8.4) for a period of t that is less than the entire pulse ($t < t_p$), the long pulse excitation response during the heating stage (SHT) at time t can be expressed as follows:

$$T^{\mathrm{SHT}}(0,t) = \int_{\tau=0}^{\tau=t} \frac{Q_0}{e\sqrt{\pi\tau}} d\tau = \frac{Q_0}{e\sqrt{\pi}} \int_{\tau=0}^{\tau=t} \frac{d\tau}{\sqrt{\tau}} = \frac{Q_0}{e\sqrt{\pi}} \left[2\sqrt{\tau} + c_1\right]_{\tau=0}^{\tau=t} = \frac{2Q_0\sqrt{t}}{e\sqrt{\pi}} \tag{8.10}$$

While by integrating the impulse response for the period of the entire pulse (t_p), the long pulse excitation response during the cooling stage (LPT) at time t ($t > t_p$) is expressed as follows:

$$\begin{aligned} T^{\mathrm{LHT}}(0,t) &= \int_{\tau=0}^{\tau=t_p} \frac{Q_0}{e\sqrt{\pi(\tau+t)}} d\tau = \frac{Q_0}{e\sqrt{\pi}} \int_{\tau=0}^{\tau=t_p} \frac{d\tau}{\sqrt{\tau+t}} \\ &= \frac{Q_0}{e\sqrt{\pi}} \left[2\sqrt{\tau+t} + c_1\right]_{\tau=0}^{\tau=t_p} = \frac{2Q_0\left(\sqrt{t_p+t} - \sqrt{t}\right)}{e\sqrt{\pi}} \end{aligned} \tag{8.11}$$

Similarly, to take into account the existence of the defect, the decay factor due to the lateral diffusion over the defect, and having a multilayer host material, Eq. (8.9) can be integrated for SHT and LPT, respectively:

$$T_d^{\mathrm{SHT}}(0,t) = \int_{\tau=0}^{t} \frac{Q_0}{e\sqrt{\pi\tau}} \left\{1 + \left[2\sum_{n=1}^{\infty} R^n \left(e^{-\frac{(nl)^2}{\alpha\tau}} - e^{-\frac{(nL)^2}{\alpha\tau}}\right)\right]\left(1 - e^{-\frac{\left(\frac{D}{2}\right)^2}{4m\alpha\tau}}\right)\right\} d\tau \tag{8.12}$$

$$T_d^{\mathrm{LHT}}(0,t) = \int_{\tau=0}^{t_p} \frac{Q_0}{e\sqrt{\pi(\tau+t)}} \left\{1 + \left[2\sum_{n=1}^{\infty} R^n \left(e^{-\frac{(nl)^2}{\alpha(\tau+t)}} - e^{-\frac{(nL)^2}{\alpha(\tau+t)}}\right)\right]\left(1 - e^{-\frac{\left(\frac{D}{2}\right)^2}{4m\alpha(\tau+t)}}\right)\right\} d\tau \tag{8.13}$$

which their solutions for SHT and LPT are as follows, respectively:

$$T_d^{\mathrm{SHT}}(0,t) = \frac{2Q_0\sqrt{t}}{e\sqrt{\pi}} + \frac{2Q_0}{e\sqrt{\pi}} \sum_{n=1}^{\infty} R^n \left[f_{(\tau,c_l)} - f_{(\tau,c_L)} - f_{(\tau,c_D+c_l)} + f_{(\tau,c_D+c_L)}\right]_{\tau=0}^{\tau=t} \tag{8.14}$$

$$\begin{aligned} T_d^{\mathrm{LHT}}(0,t) &= \frac{2Q_0\left(\sqrt{t_p+t} - \sqrt{t}\right)}{e\sqrt{\pi}} \\ &+ \frac{2Q_0}{e\sqrt{\pi}} \sum_{n=1}^{\infty} R^n \left[f_{(\tau+t,c_l)} - f_{(\tau+t,c_L)} - f_{(\tau+t,c_D+c_l)} + f_{(\tau+t,c_D+c_L)}\right]_{\tau=0}^{\tau=t_p} \end{aligned} \tag{8.15}$$

where $\left[f_{(\tau,c)}\right]_{\tau_1}^{\tau_2} = f_{(\tau_2,c)} - f_{(\tau_1,c)}$ and $f_{(\tau,c)}$ as well as the coefficients c_l, c_L, c_D are as follows:

$$f_{(\tau,c)} = 2\sqrt{\tau}e^{\frac{c}{\tau}} - 2\sqrt{\pi}\sqrt{c}\left[erfi\left(\frac{\sqrt{c}}{\sqrt{\tau}}\right)\right] + c_2 = 2\sqrt{\tau}e^{\frac{c}{\tau}} + i4\sqrt{c}\int_0^{\frac{\sqrt{c}}{\sqrt{\tau}}} e^{-\xi^2}d\xi + c_2 \tag{8.16}$$

$$c_l = -\frac{(nl)^2}{\alpha};\ c_L = -\frac{(nL)^2}{\alpha};\ c_D = -\frac{(D/2)^2}{4m\alpha} \tag{8.17}$$

where erf$i$(.) is the imaginary error function and the integral constant, c_2, will be eliminated following subtraction.

8.4.1.1 Data processing algorithms

The aforementioned analytical responses to the direct heat conduction problems are valuable for better understanding thermography inspection and even serve as inspiration for tackling the real problem of damage characterization by IRT. However, since damage identification by any NDT technique is an inverse problem for which there are no exact solutions, quantitative parameters of dynamic heat transfer and data processing algorithms are of interest in approximating the available optimal solutions to the inverse problem. To deal with the phenomenon of uneven heating/absorption, a number of contrast parameters have been proposed, including absolute (AC), running (RC), normalized (NC), and differentiated (differentiated absolute contrast, DAC) thermal contrasts (Vavilov & Burleigh, 2020). Table 8.2 lists these contrast indicators. The original output signal $S_{(T,p,t)}$ from the IR camera, which depends on the temperature T, time t, and optical properties p of the object to be inspected, is employed in these methods for analyzing data. Superscripts d and nd indicate defective and nondefective regions, respectively.

Background nonuniformity cannot be rectified using absolute thermal contrast (AC). As a result, other contrast parameters such as AC, RC, and NC have been suggested; however, these methods need to find the temperature in a region without defects. This is a serious shortcoming in these approaches. The DAC was suggested as an alternative to this problem. Using the 1D solution of the Fourier equation, this method determines the temperature in the sound region. However, DAC is a 1D approximation and is only applicable for shallow defects, a semiinfinite sample, and Dirac pulse heating. The 1D normalization method incorporates a time dimension that reduces the effects of uneven heating and surface chaos. The discretized 3D model of heat diffusion is taken into account by the 3D normalization method. This allows for the construction of a synthetic image sequence for the nondefective region of the specimen. The associated experimental original sequence can be normalized using this sequence, and lateral heat diffusion effects can be removed (Vavilov & Burleigh, 2020).

Despite the simplicity and benefits of the thermal contrast parameters, the complexity of IR inspection necessitates more complex processing and data analysis

Table 8.2 Different thermal contrast parameters for IRT inspection.

Thermal contrast parameter's name	Equation
Absolute thermal contrast	$AC_{(T,p,t)} = S^{d}_{(T,p,t)} - S^{nd}_{(T,p,t)}$
Running temperature contrast	$RC_{(T,p,t)} = \frac{AC_{(T,p,t)}}{S^{nd}_{(T,p,t)}}$
Normalized temperature contrast	$\mathrm{NC}_{(T,p,t)} = \frac{S^{d}_{(T,p,t)}}{S^{d}_{(T,p,t_h)}} - \frac{S^{nd}_{(T,p,t)}}{S^{nd}_{(T,p,t_h)}};\ t_h = \arg\max_{t \geq 0} T(t)$
Differentiated absolute contrast	$\mathrm{DAC}_{(T,p,t)} = S_{(T,p,t)} - S_{(T,p,0)} - \sqrt{\frac{t'}{t}}\left(S_{(T,p,t')} - S_{(T,p,0)}\right)$ t' is the time before the first defect becomes visible on the (thermogram) surface.
1D normalization	$N^{1D}{}_{(T,p,t)} = \frac{S_{(T,p,t)} - S_{(T,p,0)}}{S^{N}_{(T,p,t)} - S_{(T,p,0)}}$ The superscript N indicates the signal corresponding to the normalizing image.
3D normalization	$N^{3D} = \frac{S_{(T,p,t)}}{T^{\mathrm{theor}}_{nd}(T,p,t)} = \frac{T^{\mathrm{theor}}_{nd}(T,p,t) + \Delta T_{(T,p,t)}}{T^{\mathrm{theor}}_{nd}(T,\,p,\,t)}$ $\mathrm{T}^{\mathrm{theor}}_{\mathrm{nd}}$ is the theoretical temperature function for a nondefective area achieved by solving the corresponding 3D Thermal NDT problem.

algorithms, particularly for composite laminates with complicated structures that may contain a variety of defects. PPT, one of the primary algorithms used to post-process PT thermograms, utilizes analysis of phase in the frequency domain and is a signal processing technique that softens imperfections of heating unevenness (Ishikawa et al., 2013). PPT uses low frequencies, usually up to 2−3vHz, to detect deeper flaws. The Fourier Transform is the basis for the method used for obtaining the phase from the thermograms:

$$\hat{T}_n = \Delta t \sum_{k=1}^{N} S_{(T,p,k\Delta t)} e^{\left(-\frac{j2\pi kn}{N}\right)} = \mathrm{Re}_n + jIm_n \tag{8.18}$$

where Δt is the interval time of sampling, j is the imaginary number, N is the total number of thermograms (frequencies), and n is the investigated frequency. Re_n and Im_n are the real and imaginary parts of the Fourier transform for the frequency n, respectively. The amplitude (A_n) and phase (ϕ_n) of the different frequencies are calculated using Eq. (8.19):

$$A_n = \sqrt{\mathrm{Re}_n{}^2 + \mathrm{Im}_n{}^2};\quad \phi_n = \tan^{-1}\left(\frac{Im_n}{\mathrm{Re}_n}\right) \tag{8.19}$$

where phase (ϕ_n) is commonly examined for PPT. The term "blind frequency" f_b is frequently utilized in PPT assessment to describe the inhibiting frequency at which the defect creates insufficient phase contrast to be observed on the phase spectrum. Eq. (8.20) is a typical correlation between "blind frequency" and defect depth l:

$$l = C_1\sqrt{\frac{\alpha}{\pi f_b}} \tag{8.20}$$

where the so-called "correlation constant" C_1 has a range of 1.5 to 2 (Castanedo, 2005).

Thermal signal reconstruction (TSR), another popular approach for processing thermal data, was originally developed for the PT and is based on applying the logarithm function to Eq. (8.4), which extends as follows (Shepard et al., 2002):

$$\ln(T(0,t)) = \ln\left(\frac{Q_0}{e}\right) - \frac{1}{2}\ln(\pi t) \tag{8.21}$$

According to Eq. (8.21), there is a linear correlation between time and temperature in the logarithmic domain with a slope of $-1/2$. The thermal response is consequently disturbed by various factors, such as background radiation, imperfect dirac excitation, finite-thickness material, 3D heat diffusion, etc., and thus the linear correlation is not perfectly satisfied by Eq. (8.21) as it should be. Consequently, in order to estimate the logarithmic temperature evolution, Eq. (8.22) allows the use of an n-degree polynomial function:

$$\ln(T(0,t)) = a_0 + a_1\ln(\pi t) + a_2[\ln(\pi t)]^2 + \ldots + a_n[\ln(\pi t)]^n \tag{8.22}$$

Due to the significant improvements in noise reduction offered by the TSR approach, smaller and deeper defects have been observed (Shepard et al., 2003). These functions' first- and second-time derivative images can also be taken into consideration because they might yield results that are clearer than raw data images (Roche & Balageas, 2015).

Another prevalent and practical algorithm for processing thermograms is PCT, which applies singular value decomposition to a thermal image sequence and adjusts the well-known principal component analysis (PCA) algorithm (Rajic, 2002). In PCT, a series of thermal images in a 3D matrix is first converted to a 2D matrix where each column is a reshaped thermal image. The output, after PCA has been applied to this 2D matrix, is then reformed by reshaping each column to the prior size of a thermal image.

Roche and Balageas (2015) compared SHT and PT in order to identify damage within CFRP composite laminates that were located at various depths. Without any sort of processing algorithm applied to either of the thermographic techniques (during visual inspection), SHT was able to detect surface flaws but not deep damage. TSR, on the other hand, improved the contrast and allowed for a better

identification of damage when used with the PT technique. However, since the relative values of effective excitation energy are not provided, it is impractical to determine for sure whether PT or SHT is fundamentally superior. Almond et al. (2017) employed PT and LPT to examine four typical engineering materials: aluminum alloy, mild steel, stainless steel, and CFRP, all of which had a defect of the same diameter of 5 mm that was located 1 mm below the surface. The findings demonstrated that the LPT is effective for detecting defects in materials with low thermal conductivity/diffusivity, such as GFRP and CFRP, but less effective for materials with high thermal conductivity/diffusivity, particularly for shallow defects. However, the LPT is still expected to be more effective in the case of deeper defects in materials with high thermal conductivity/diffusivity. The PT method, in contrast, is just as beneficial at finding shallow flaws in both kinds of materials, but the images it generates are noisier and have less contrast than those from LPT. Only when the peak contrast time is considerably shorter than 1 second does the LPT's efficiency noticeably decrease. Peak contrast time is influenced by defect depth and diameter, as well as thermal characteristics. As a result, the peak contrast time of a very shallow defect in a low thermal conductivity material may be much shorter than 1 second, causing the LPT less effective for its identification. Likewise, a deep defect in a material with high thermal conductivity can result in a peak contrast time of close to or greater than a second, making LPT more appropriate. On the other hand, the PT's application is restricted to the use of high-pulse-energy optical flash lamps with a very high-intensity flash of light emitting for a duration of 1−2 ms. This equipment is also much more expensive (approximately 100 times (Almond et al., 2017)) than LPT/SHT's.

The effective period, which includes the number of thermograms with high contrasts, is shorter for PT compared to SHT and LPT, despite the fact that the achieved contrast in PT may be higher than that of SHT or LPT. In light of this, the thermal signal area (TSA), a cumulative processing algorithm of these thermograms, has been developed, resulting in a unique thermal map (Moradi & Safizadeh, 2019a). TSA uses the integration of each pixel's temperature over time, which has acceptable contrast and is less sensitive to transient noise (e.g., at the peak contrast time). Optimizing the range of integration in TSA, which should be from somewhere in the heating phase to somewhere in the cooling phase (combining SHT and LPT), is crucial for delivering higher performance given that this is when the contrasts for defects at various possible depths are expected to begin and end, respectively. Therefore, the lower and upper integral limits should be set, respectively, after beginning the heating and before reaching the steady state. Taking inspiration from TSA's use of integral calculations in the time domain, the potential of the frequency domain can be explored. In this regard, the adaptive spectral band integration (ASBI) algorithm was developed, where the phase contrast is integrated over the pertinent frequency range pixel-wise as opposed to frame-wise for TSA (Poelman et al., 2020). The frequency domain range in ASBI where the pixel's phase contrast is negative (between the first and second blind frequencies) determines the integration limits, maximizing defect detectability and yielding an almost zero-reference level. A CFRP sample with flat bottom holes and BVID, as

well as an aircraft CFRP panel (Airbus A400M) with backside stiffeners and a complex cluster with manufacturing defects, were examined in order to verify the ASBI algorithm's efficiency.

8.4.2 Sinusoidal amplitude modulation

In LIT, after a harmonic excitation of a particular frequency for several cycles (Fig. 8.1C) to generate heat penetration into the corresponding diffusion length, the amplitude and phase of the thermal response during heating are calculated, with the latter being a relatively emissivity-normalized quantity (Hedayatrasa et al., 2019). For harmonic heat emitted on an opaque and homogeneous plate with the geometry of Fig. 8.2, the heat flux distribution of the source is $\left(Q_0/2\right)[1+\cos(\omega t)] = \mathrm{Re}\left\{\left(Q_0/2\right)[1+\exp(j\omega t)]\right\}$, which is proper to generate a continuous sinusoidal wave with $\omega = 2\pi f$ as the angular modulation frequency. This heat flux function includes two portions: DC thermal increase $(Q_0/2)$ and AC thermal modulation $(\left(Q_0/2\right)\cos(\omega t) = \left(Q_0/2\right)\exp(j\omega t))$. Given this heat flux distribution and material properties, the analytical solution of Eq. (8.2) will be in the form of (Bai & Wong, 2001):

$$T(z,t) = \underbrace{T_{DC}(z)}_{\text{DC component}} + \underbrace{T_{AC}(z)\exp(j\omega t)}_{\text{AC component}} \tag{8.23}$$

Discarding the exponential time factor, the general solution of Eq. (8.2) for the harmonic heat flux is

$$T_{AC}(z) = A.\exp\left(-\frac{(1+j)}{\mu}z\right) + B.\exp\left(\frac{(1+j)}{\mu}z\right) \tag{8.24}$$

where $\mu = \sqrt{2\alpha/\omega} = \sqrt{\alpha/\pi f}$ denotes the thermal wave diffusion length. A and B are constants that can be determined using the boundary condition equations. Detailed analytical solutions for the evaluation of defects in composite plates using LIT can be found in Bai and Wong (2001). It should be noted that the solution to the DC component is found in Section 8.3.1. Moreover, a new practical technique, so-called "phase inversion thermography (PIT)", to extract the AC component from the thermal response for LIT and FM/PM was introduced (Hedayatrasa et al., 2022).

8.4.3 Frequency-phase modulation

In the field of IRT, different types of excitation-modulated waveforms have been utilized. These include analog frequency modulation (FM) or sweep signals, discrete phase modulation (PM) such as Barker binary coding, and FPM or angle modulation waveforms (Hedayatrasa et al., 2019, 2021). As previously mentioned, LIT is a subset of AM with a longer history in IRT; nonetheless, modulated waveforms are provided separately to facilitate discussion of the concepts. In fact, modulated waveforms refer to angle modulation, including FM, PM, and FPM, rather than

AM. Similar to LIT, for FPM, the heat flux distribution of the source can be formulated as $(Q_0/2)\left[1+\exp\left(j\left(\omega t+\pi Bt^2/\tau\right)\right)\right]$ or, for FM, $Q_0\left[1+\sin\left(\omega t+\pi Bt^2/\tau\right)\right]$, where B is the bandwidth of probing thermal waves and τ is the duration of excitation. For further details, an analytical study considering a case of CFRP under FM thermal wave imaging (FMTWI) for defect depth estimation can be found in Rani et al. (2023). Also, PT, LIT, and FMTWI methods were compared for a CFRP board containing artificial defects in Chatterjee et al. (2011).

Tabatabaei and Mandelis (2011) conducted a study to investigate the enhanced depth resolution of TWR using Barker binary-coded excitation waveforms. They demonstrated the capability of this technique for deconvolving thermal responses from overlapping defects in an experimental setup (Tabatabaei & Mandelis, 1989). Researchers have explored the use of excitation signals with analog FM (such as sweep signals) or discrete PM (like Barker-coded signals) in IRT. In 2019, a novel FPM waveform was introduced (Hedayatrasa et al., 2019), aiming at an optimized excitation signal for improved TWR imaging. They conducted a comparative analysis with other types of excitation signals, including AM (classical lock-in), FM (sweep), and PM (Barker-coded) signals, all with the same duration as the FPM waveform.

8.5 Case studies

This section focuses on the investigation of two CFRP samples with BVID using flash thermography (OPT). The purpose is to demonstrate the potential of IRT in inspecting composite structures after impact loading. The first sample is a CFRP laminate that underwent controlled impact using a drop tower, resulting in BVID. Fig. 8.3A displays a photograph of the first sample. The second CFRP sample is a section specifically manufactured for the vertical stabilizer of an Airbus A320 aircraft. On the underside of this sample, there are clearly visible stiffeners that are bonded to a base plate that is 4 mm thick. A photograph of the second sample can be found in Fig. 8.3B. The material's elastic properties and densities remain unknown. The second sample experienced three impacts, resulting in three distinct areas of BVID labeled as BVID-A, BVID-B, and BVID-C, respectively. Figs. 8.3C and D present the C-scans of both samples, illustrating the impact damage. The first sample allows for a closer examination of delaminations occurring at different interfaces. Its C-scan (time-of-flight map) exposes eight levels of defects, as depicted in Fig. 8.4. These defects resemble a winding staircase, with steps occurring at 45 degrees intervals. Only the margins of defects no. 6 to no. 8 are visible. Further details regarding the experimental parameters and setup adjustments for both samples can be found in Table 8.3.

The thermal data undergoes initial pre-processing steps, which include spatial cropping, subtracting the cold image, removing saturated frames, converting digital values to degrees Celsius (°C), and temporal standardization. Following that, various algorithms, including TSR, PPT, PCT, TSA, and ASBI, are used to postprocess the thermograms. All results are presented using logarithmic scales for better

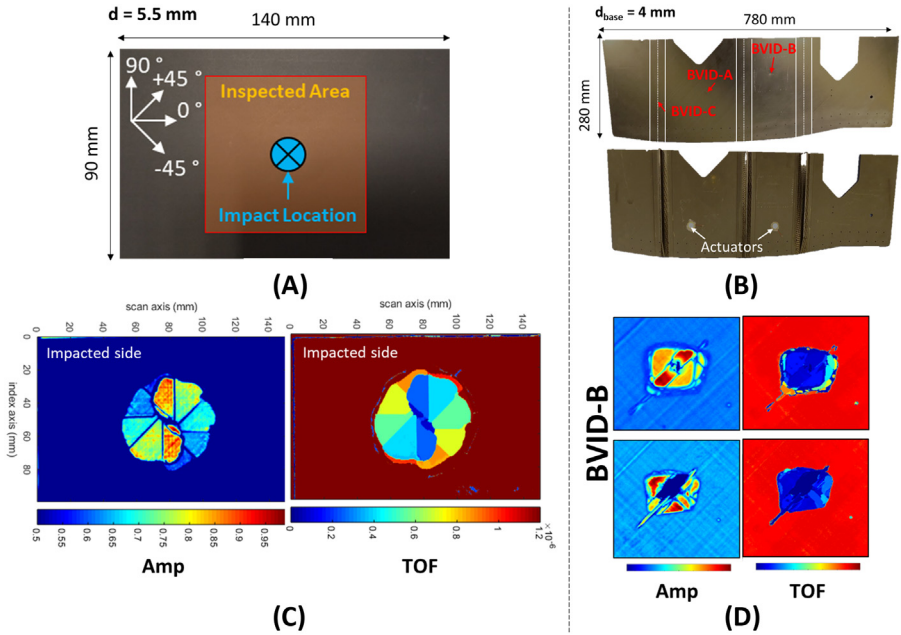

Figure 8.3 The schematic drawing of the (A) CFRP coupon and (B) CFRP aircraft panel, both with BVID and impacted at one and three locations, respectively, alongside their C-scans in (C) and (D).
Source: Modified from Poelman, G., Hedayatrasa, S., Segers, J., Van P., Wim & Kersemans, M. (2020). Adaptive spectral band integration in flash thermography: Enhanced defect detectability and quantification in composites. *Composites Part B: Engineering*, *202*. https://doi.org/10.1016/j.compositesb.2020.108305 and Segers, Joost, Hedayatrasa, Saeid, Poelman, G., Van P., Wim, & Kersemans, M. (2022). Self-reference broadband local wavenumber estimation (SRB-LWE) for defect assessment in composites. *Mechanical Systems and Signal Processing*, *163*, 108142. https://doi.org/10.1016/j.ymssp.2021.108142.

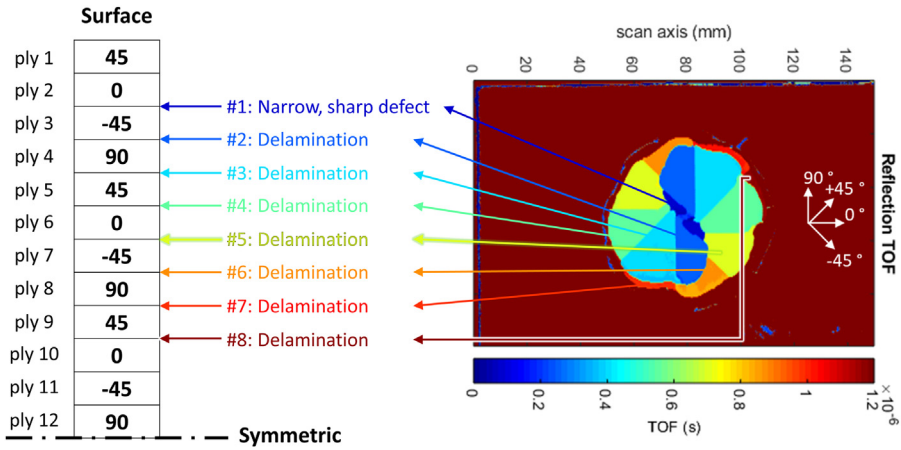

Figure 8.4 Eight levels of defects (delaminations), based on the C-scan (time-of-flight map), for the first CFRP sample after impact.

Table 8.3 Experimental setup and parameters for two case studies.

Experimental parameters		**1st sample**	**2nd sample**
Composite	Material Layup Dimension	CFRP plate $[(+45/0/-45/90)_3]_s$ $140 \times 90 \times 5.5$ mm^3	CFRP panel cross-ply $780 \times 280 \times 4$ mm^3
Impact	Impactor's weight Dropping height Energy	7.72 kg 30 cm 18.5 J	7.1 kg 20, 35, and 30 cm 14, 24, and 21 J
Excitation source	Source type Excitation duration Excitation Energy	Hensel linear flash lamp 5 ms 6 kJ	Hensel linear flash lamp 5 ms 6 kJ
Distance between the **Excitation source** and the inspected **sample**		~300 mm	~500 mm
IR camera	Sensor type Wavelength Sensor resolution Frame rate NEDT	Cryo-cooled InSb detectors 3–5 μm 640×512 50 Hz ≤ 20 mK	Cryo-cooled InSb detectors 3–5 μm 640×512 30 Hz ≤ 20 mK
Distance between the **IR camera** and the inspected **sample**		~500 mm	~800 mm
Recording duration by the **IR camera**		50 s	40 s

visualization, unless specified otherwise. To achieve the logarithmic scale, the phase contrast map's sign is inverted, and all phase contrast values are made positive by adding the minimum value of the resulting phase contrast map. Finally, the decimal logarithm of the values is calculated.

In Fig. 8.5, the outcome of the TSR algorithm and its first and second derivatives for the first CFRP sample at various points in time (frames) are displayed. From the results of TSR itself, defects no. 2 (at 0.02, 0.1, and 2 seconds), no. 3 (at 0.02, 0.2, and 2 seconds), and no. 4 (at 0.2 seconds) can be detected. On the other hand, defect no. 1 can be detected at 0.2 seconds of the second derivative. The overall delaminated area (circle) covering delaminations at different interfaces, regardless of their depth locations, can also be distinguished in TSR (at 1 second), the first derivative of TSR (at 1 and 2 seconds), and the second derivative of TSR (at 0.2 and 0.4 seconds).

The results of the PCT method (three principal components of 2, 3, and 10) and the PPT algorithm at frequencies of 0.12, 0.20, and 0.50 Hz are shown in Fig. 8.6. The overall defective region (0.12 Hz) and defects no. 2, no. 3, and no. 4 (0.20 and 0.50 Hz) may be identified from the PPT details. The overall delaminated circle

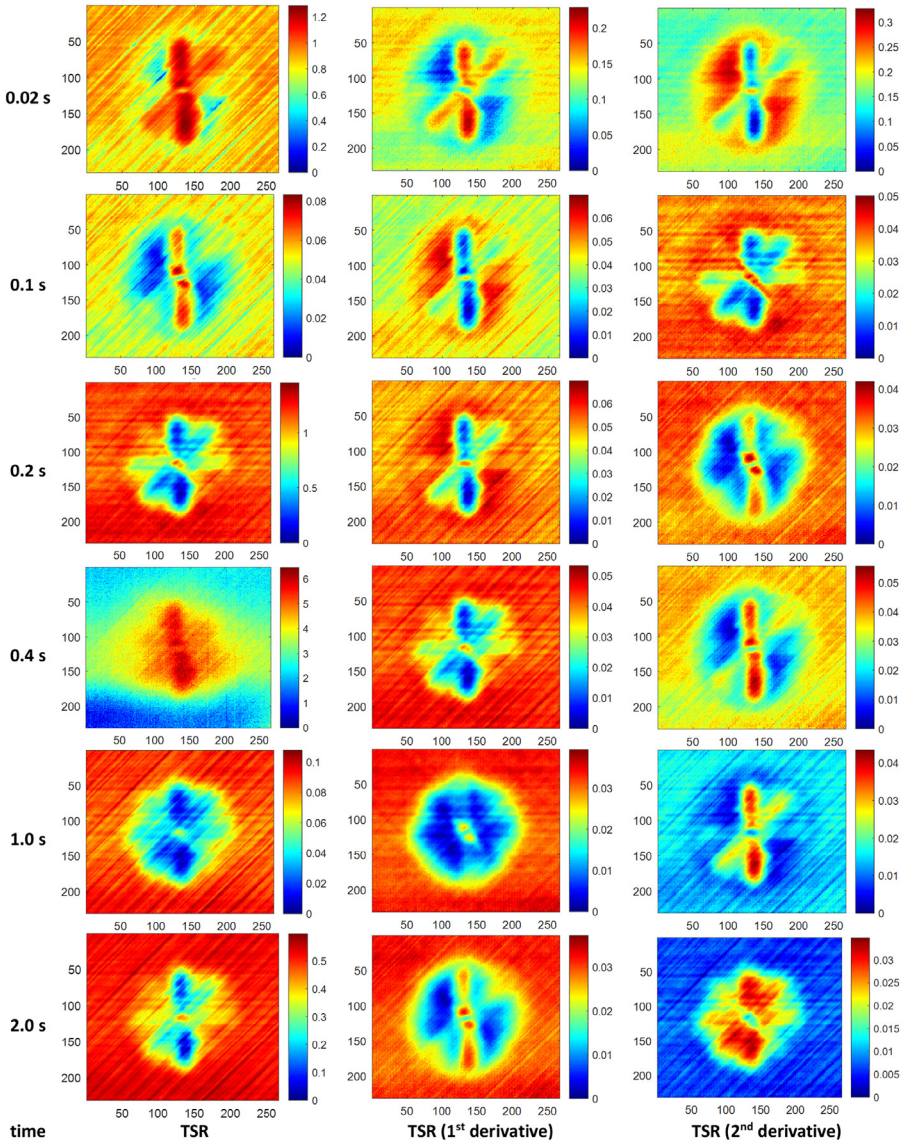

Figure 8.5 Results of TSR and its first and second derivatives for the first CFRP sample at various times.

may be derived from PCT; however, defects no. 2, no. 3, and no. 4 are more challenging to individualize.

To apply the TSA algorithm, the limits of the integral in the temporal domain should exclude the steady state phase. This temporal integral range can still be optimized to include a high ratio of informative thermograms to uninformative-noisy

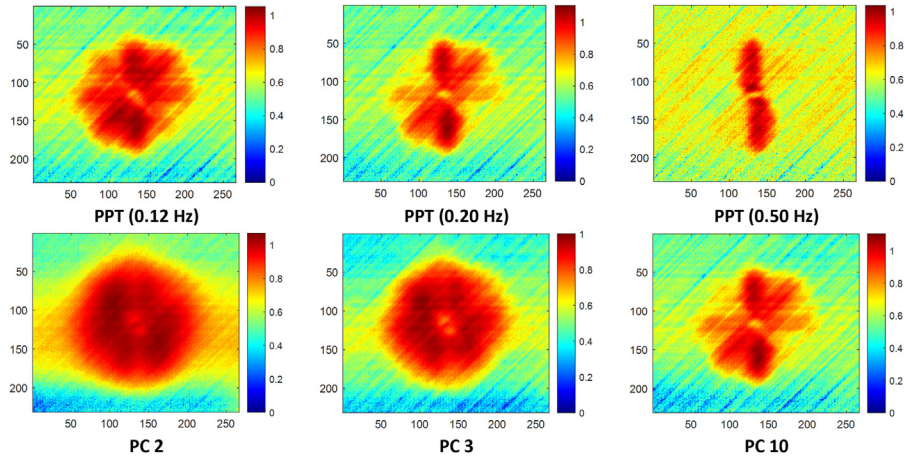

Figure 8.6 Results of PPT and PCT for the first CFRP sample.

ones. For flash thermography, this integral can start at the first moment (frame) following the flash and be continued with various lengths of window (LoW). The absolute value of the gradient of mean temperature (averaged over all pixels in each frame) can be used to calculate the upper integral limit ($|dT/dt| > \delta$). When this parameter drops to a certain level δ (either equal to or below a threshold), the upper limit can be reached. In Fig. 8.7, for instance, the TSA's outcomes for thresholds (δ) of 0.2 (end time 0.3 seconds—frame 15), 0.05 (end time 0.82 seconds—frame 41), 0.025 (end time 1.34 seconds—frame 67), and 0.013 (end time 2.12 seconds—frame 106) are shown. Defects no. 1 and no. 2, the overall damaged circle, and a shadow of defect no. 3 are visible, despite the fact that TSA intends to be more advantageous for SHT and LPT than PT.

To compare the results of operating the integral in the frequency domain (ASBI) with the time domain (TSA), the findings of ASBI are shown in Fig. 8.7 in both linear and logarithmic scales. This technique allows for the segregation of defects no. 1 and no. 2, the overall damaged circle, and a shadow of defect no. 3. It should be noted that it is not necessary to set a lower limit for the TSA's integral immediately following an optical flash. Fig. 8.8 shows the outcomes when three LoWs of 0.1, 0.2, and 1 seconds (5, 10, and 50 frames) are used as the integral range and four different lower bounds for the TSA's integral are used (at the 10th, 60th, 90th, and 120th frame). The damaged area, highlighted by defect no. 1, may first be seen with LoW of 5 (0.1 second) and 10 (0.2 second) frames. Later, defects no. 2, no. 3, and no. 4, as well as a shadow of defect no. 5, are added. With a LoW of 50 (1 second), it begins by displaying defect no. 2 and at a lower resolution.

The second sample, which is bigger than the first, can be analyzed to locate the overall BVID zones. For the second CFRP component, the results of the TSR algorithm and its first and second derivatives are shown in Fig. 8.9 at various points in time. The three BVID zones are more clearly visible at 1 second using the TSR and its second derivative than at other times.

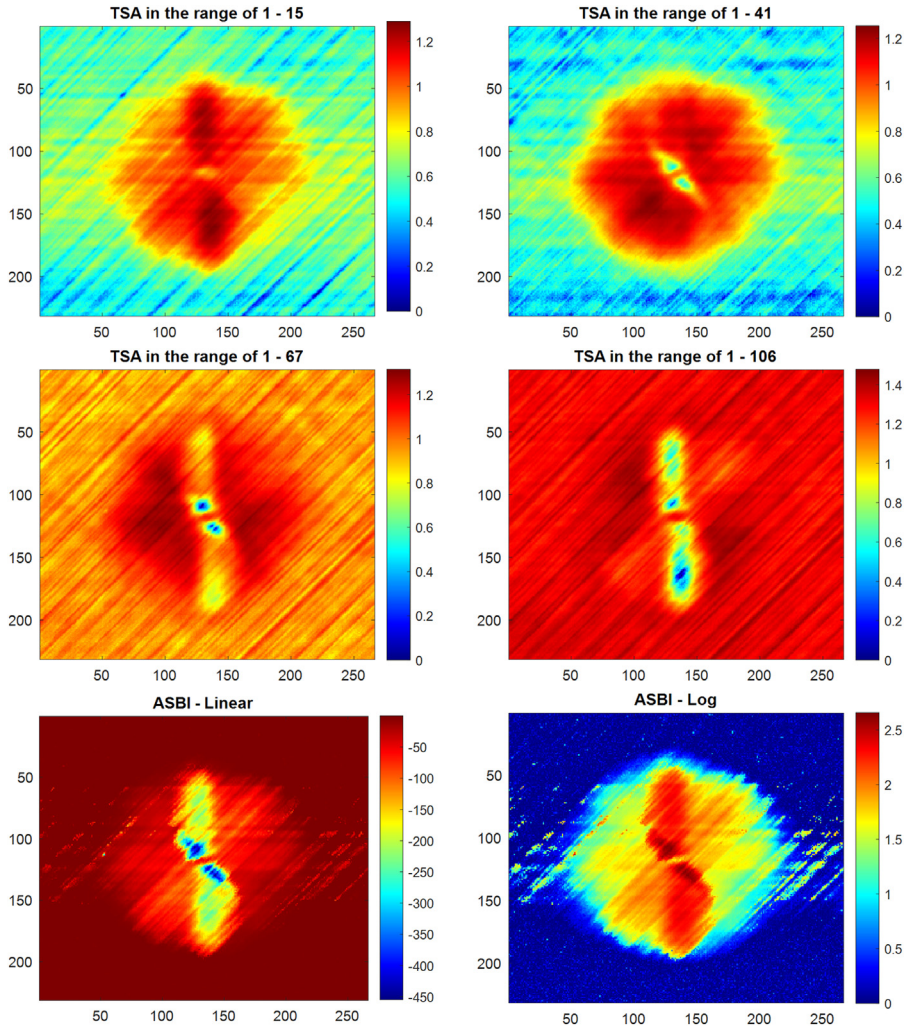

Figure 8.7 Results of TSA with integral ranges starting from the flash and ASBI for the first CFRP sample.

Fig. 8.10 displays the outcomes of the PPT algorithm at frequencies of 0.05, 0.125, and 0.475 Hz and the PCT method (three principal components of 2, 3, and 6). BVID C is less visible than BVIDs A and B.

In Fig. 8.11, the TSA's outcomes for thresholds (δ) of 0.2 (end time 0.367 second—frame 12), 0.1 (end time 0.6 second—frame 19), 0.05 (end time 1 second—frame 31), and 0.025 (end time 13.17 second—frame 396) are shown. The TSA was capable of discovering all three BVIDs. The ASBI, however, was able to distinguish them more clearly, as illustrated in Fig. 8.11.

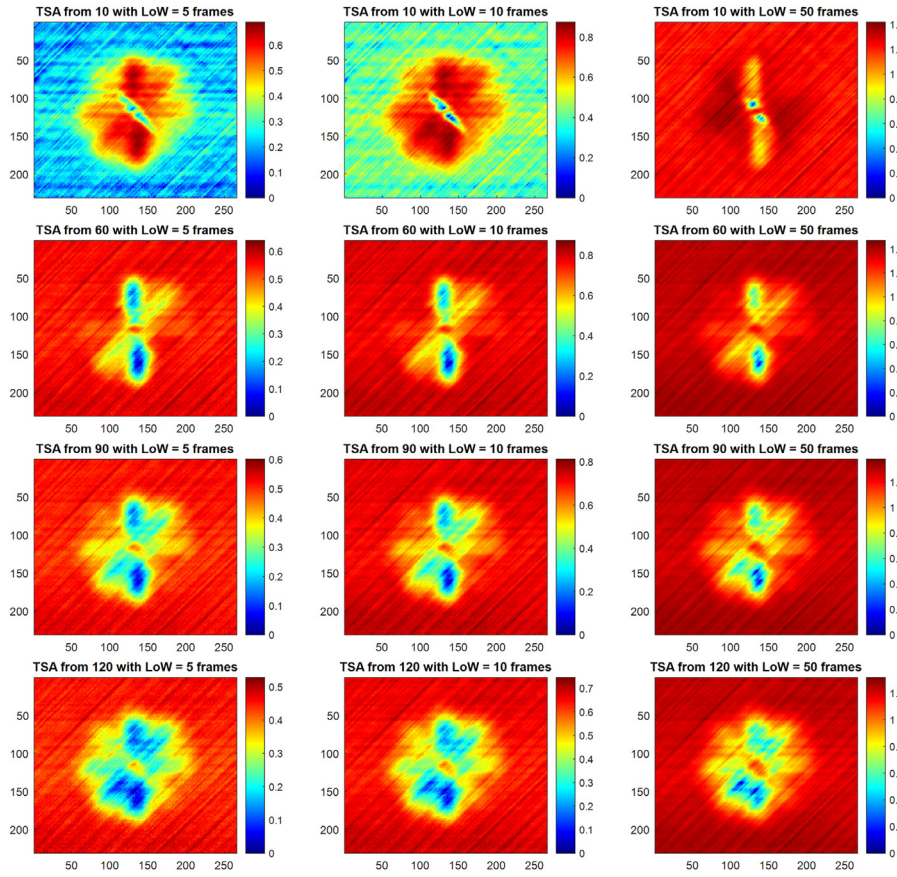

Figure 8.8 Results of TSA using integral ranges with three length of windows (LoWs) of 5, 10, and 50 frames and starting at various frames.

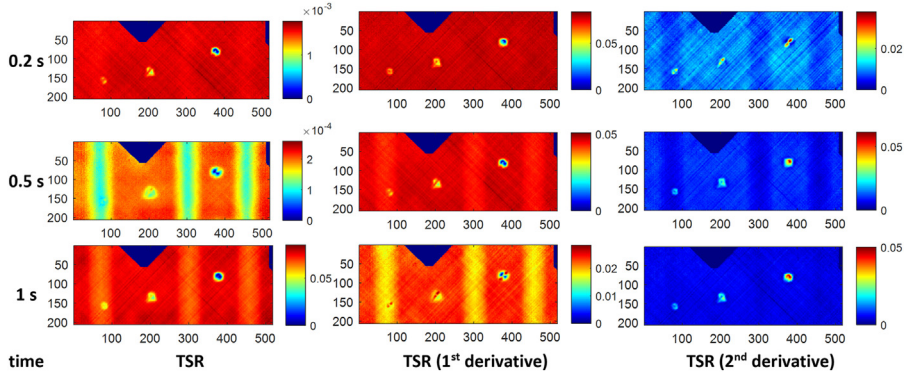

Figure 8.9 Results of TSR and its first and second derivatives for the second CFRP sample at various times.

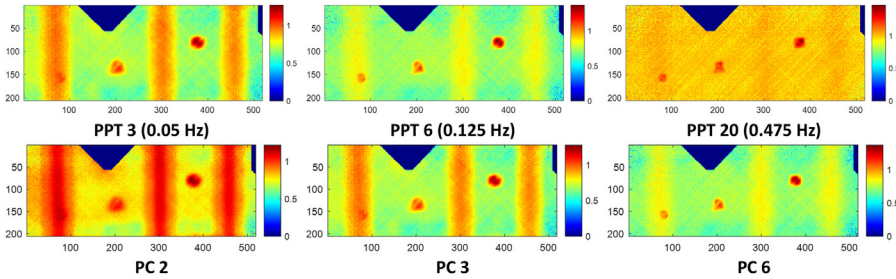

Figure 8.10 Results of PPT and PCT for the second CFRP sample.

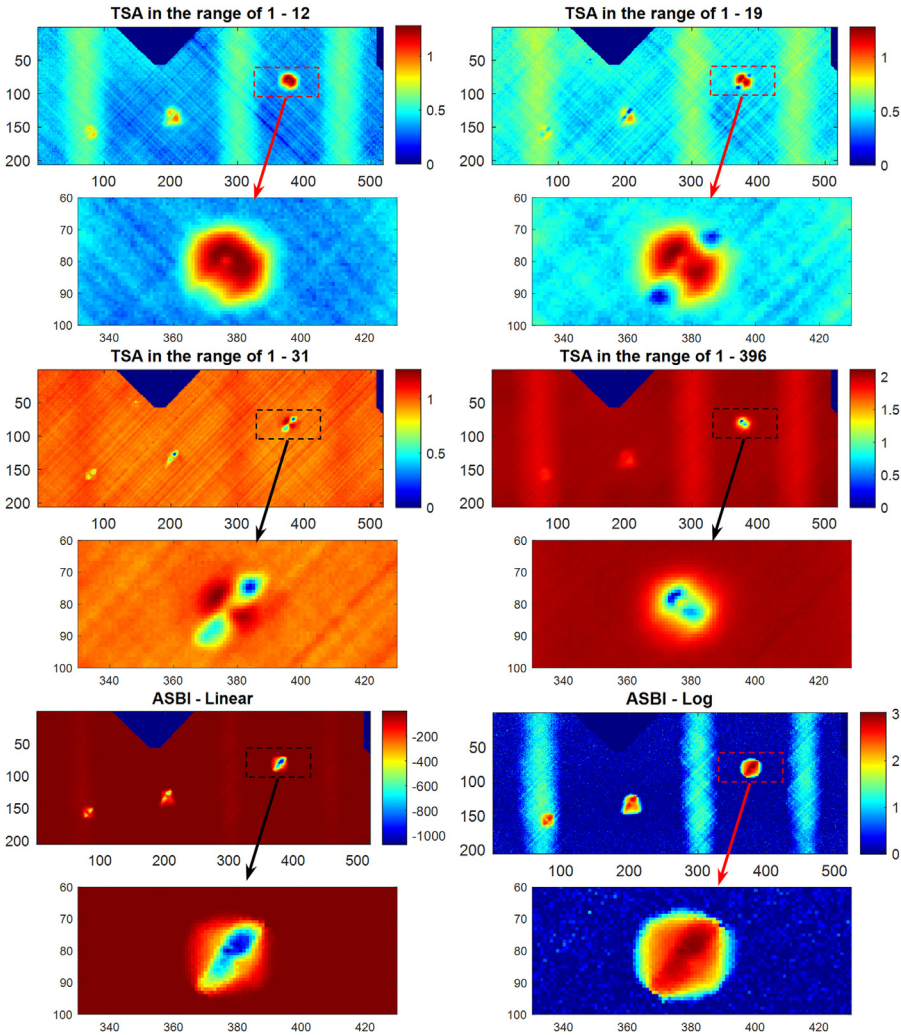

Figure 8.11 Results of TSA with integral ranges starting from the flash and ASBI for the second CFRP sample.

The results demonstrate that IRT has the capability to identify impact damages in composite structures. It is effective in closely inspecting and differentiating delaminations at various layers to some extent, as observed in the first CFRP sample. Additionally, IRT is suitable for conducting inspections from a distance, particularly for larger components like the second CFRP sample, to identify zones affected by BVIDs. By utilizing and optimizing advanced equipment for heat excitation and thermogram recording, as well as employing more sophisticated algorithms, particularly those based on AI, the reliability and performance of IRT can be further enhanced. These advancements have the potential to improve the accuracy and effectiveness of impact damage detection in composite structures.

8.6 Conclusions

This Chapter has focused attention on assessing impact damage in composite laminates via IRT. After a brief review of this matter, active IRT methodologies based on excitation sources (optically, mechanically, and inductively stimulated thermography), heating waveforms (step and pulse, sinusoidal amplitude modulated and frequency-phase modulated waveforms) and data processing, case studies, and related discussions have accurately been deepened by the authors. Concerning the case studies section, it fo cused on the investigation of two CFRP samples with BVID using flash thermography. The IRT technique was found effective in inspecting and differentiating between delaminations at various layers, as observed in the first impacted CFRP sample. The inspection of the impacted CFRP aircraft panel showed the potential of the IRT technique for industrial implementation. It is finally reasonable to think that by utilizing and optimizing advanced equipment for heat excitation and thermogram recording, as well as employing more sophisticated algorithms, particularly those based on AI, the reliability and performance of IRT can be further enhanced.

References

Alhammad, M., Avdelidis, N. P., Ibarra-Castanedo, C., Torbali, M. E., Genest, M., Zhang, H., Zolotas, A., & Maldgue, X. P. V. (2022). Automated impact damage detection technique for composites based on thermographic image processing and machine learning classification. *Sensors*, *22*(23). Available from https://doi.org/10.3390/s22239031.

Almond, D. P., Angioni, S. L., & Pickering, S. G. (2017). Long pulse excitation thermographic nondestructive evaluation. *NDT and E International*, *87*, 7−14. Available from https://doi.org/10.1016/j.ndteint.2017.01.003.

Almond, D. P., & Pickering, S. G. (2012). An analytical study of the pulsed thermography defect detection limit. *Journal of Applied Physics*, *111*(9). Available from https://doi.org/10.1063/1.4704684.

Avdelidis, N. P., Almond, D. P., Dobbinson, A., Hawtin, B. C., Ibarra-Castanedo, C., & Maldague, X. (2004). Aircraft composites assessment by means of transient thermal

NDT. *Progress in Aerospace Sciences*, *40*(3), 143−162. Available from https://doi.org/10.1016/j.paerosci.2004.03.001.

Bai, W., & Wong, B. S. (2001). Evaluation of defects in composite plates under convective environments using lock-in thermography. *Measurement Science and Technology*, *12*(2), 142−150. Available from https://doi.org/10.1088/0957-0233/12/2/303.

Balageas, D., Bourasseau, S., Dupont, M., Bocherens, E., Dewynter-Marty, V., & Ferdinand, P. (2000). Comparison between non-destructive evaluation techniques and integrated fiber optic health monitoring systems for composite sandwich structures. *Journal of Intelligent Material Systems and Structures*, *11*(6), 426−437. Available from https://doi.org/10.1106/mfm1-c5ft-6bm4-afud.

Ball, R. J., & Almond, D. P. (1998). The detection and measurement of impact damage in thick carbon fibre reinforced laminates by transient thermography. *NDT & E International*, *31*(3), 165−173. Available from https://doi.org/10.1016/s0963-8695(97)00052-2.

Bates, D., Smith, G., Lu, D., & Hewitt, J. (2000). Rapid thermal non-destructive testing of aircraft components. *Composites Part B: Engineering*, *31*(3), 175−185. Available from https://doi.org/10.1016/s1359-8368(00)00005-6.

Bayat, M., Safizadeh, M. S., & Moradi, M. (2019). Numerical and experimental study for assessing stress in carbon epoxy composites using thermography. *Infrared Physics & Technology*, *98*, 108−113. Available from https://doi.org/10.1016/j.infrared.2019.03.003, https://doi.org/10.1016/j.infrared.2019.03.003.

Bhatt, R. T., Choi, S. R., Cosgriff, L. M., Fox, D. S., & Lee, K. N. (2008). Impact resistance of uncoated SiC/SiC composites. *Materials Science and Engineering A*, *476*(1−2), 20−28. Available from https://doi.org/10.1016/j.msea.2007.04.066.

Busse, G., Wu, D., & Karpen, W. (1992). Thermal wave imaging with phase sensitive modulated thermography. *Journal of Applied Physics*, *71*(8), 3962−3965. Available from https://doi.org/10.1063/1.351366.

Caruso, M. M., Davis, D. A., Shen, Q., Odom, S. A., Sottos, N. R., White, S. R., & Moore, J. S. (2009). Mechanically-induced chemical changes in polymeric materials. *Chem. Rev.*, *109*(11), 5755−5798. Available from https://doi.org/10.1021/cr9001353, https://doi.org/10.1021/cr9001353.

Castanedo, C. I. (2005). *Quantitative subsurface defect evaluation by pulsed phase thermography: depth retrieval with the phase* (Doctoral dissertation, Universite Laval).

Chatterjee, K., Tuli, S., Pickering, S. G., & Almond, D. P. (2011). A comparison of the pulsed, lock-in and frequency modulated thermography nondestructive evaluation techniques. *NDT and E International*, *44*(7), 655−667. Available from https://doi.org/10.1016/j.ndteint.2011.06.008.

Chen, X., Tian, G., Wu, J., Tang, C., & Li, K. (2019). Feature-based registration for 3D eddy current pulsed thermography. *IEEE Sensors Journal*, *19*(16), 6998−7004. Available from https://doi.org/10.1109/JSEN.2019.2911699, http://ieeexplore.ieee.org/xpl/RecentIssue.jsp?punumber = 7361.

Ciampa, F., Mahmoodi, P., Pinto, F., & Meo, M. (2018). Recent advances in active infrared thermography for non-destructive testing of aerospace components. *Sensors (Switzerland)*, *18*(2). Available from https://doi.org/10.3390/s18020609, http://www.mdpi.com/1424-8220/18/2/609/pdf.

Cielo, P., Maldague, X., Deom, A. A., & Lewak, R. (1987). Thermographic nondestructive evaluation of industrial materials and structures. *Materials Evaluation*, *45*(4), 452−460.

De Rosa, I. (2011). Post-impact mechanical characterisation of E-glass/basalt woven fabric interply hybrid laminates. *Express Polymer Letters*, *5*(5).

De Rosa, I. M., Santulli, C., Sarasini, F., & Valente, M. (2009). Post-impact damage characterization of hybrid configurations of jute/glass polyester laminates using acoustic emission and IR thermography. *Composites Science and Technology*, *69*(7−8), 1142−1150. Available from https://doi.org/10.1016/j.compscitech.2009.02.011.

Deng, B., Wu, W., Li, X., Wang, H., He, Y., Shen, G., Tang, Y., Zhou, K., Zhang, Z., & Wang, Y. (2022). Active 3-D thermography based on feature-free registration of thermogram sequence and 3-D shape via a single thermal camera. *IEEE Transactions on Industrial Electronics*, *69*(11), 11774−11784. Available from https://doi.org/10.1109/TIE.2021.3120471, http://ieeexplore.ieee.org/xpl/tocresult.jsp?isnumber = 5410131.

Deng, K., Liu, H., Yang, L., Addepalli, S., & Zhao, Y. (2023). Classification of barely visible impact damage in composite laminates using deep learning and pulsed thermographic inspection. *Neural Computing and Applications*, *35*(15), 11207−11221. Available from https://doi.org/10.1007/s00521-023-08293-7, https://www.springer.com/journal/521.

Dionysopoulos, D., Fierro, G. P. M., Meo, M., & Ciampa, F. (2018). Imaging of barely visible impact damage on a composite panel using nonlinear wave modulation thermography. *NDT and E International*, *95*, 9−16. Available from https://doi.org/10.1016/j.ndteint.2018.01.005.

Dyrwal, A., Meo, M., & Ciampa, F. (2018). Nonlinear air-coupled thermosonics for fatigue micro-damage detection and localisation. *NDT & E International*, *97*, 59−67. Available from https://doi.org/10.1016/j.ndteint.2018.03.012.

Favro, L. D., Han, X., Ouyang, Z., Sun, G., Sui, H., & Thomas, R. L. (2000). Infrared imaging of defects heated by a sonic pulse. *Review of Scientific Instruments*, *71*(6), 2418−2421. Available from https://doi.org/10.1063/1.1150630.

Fierro, G. P. M., Ginzburg, D., Ciampa, F., & Meo, M. (2017). Imaging of barely visible impact damage on a complex composite stiffened panel using a nonlinear ultrasound stimulated thermography approach. *Journal of Nondestructive Evaluation*, *36*(4). Available from https://doi.org/10.1007/s10921-017-0449-x, http://www.kluweronline.com/issn/0195-9298.

Garnier, C., Pastor, M. L., Eyma, F., & Lorrain, B. (2011). The detection of aeronautical defects in situ on composite structures using non destructive testing. *Composite Structures*, *93*(5), 1328−1336. Available from https://doi.org/10.1016/j.compstruct.2010.10.017, http://www.sciencedirect.com.

Gros, X. E., Bousigue, J., & Takahashi, K. (1999). NDT data fusion at pixel level. *NDT & E International*, *32*(5), 283−292. Available from https://doi.org/10.1016/s0963-8695(98)00056-5.

Hansen, U. (1999). Damage development in woven fabric composites during tension-tension fatigue. *Journal of Composite Materials*, *33*(7), 614−639. Available from https://doi.org/10.1177/002199839903300702.

He, Y., Deng, B., Wang, H., Cheng, L., Zhou, K., Cai, S., & Ciampa, F. (2021). Infrared machine vision and infrared thermography with deep learning: A review. *Infrared Physics & Technology*, *116*. Available from https://doi.org/10.1016/j.infrared.2021. 103754.

He, Y., Tian, G., Pan, M., & Chen, D. (2014). Impact evaluation in carbon fiber reinforced plastic (CFRP) laminates using eddy current pulsed thermography. *Composite Structures*, *109*(1), 1−7. Available from https://doi.org/10.1016/j.compstruct.2013.10.049, http://www.elsevier.com/inca/publications/store/4/0/5/9/2/8.

He, Y., & Yang, R. (2015). Eddy current volume heating thermography and phase analysis for imaging characterization of interface delamination in CFRP. *IEEE Transactions on Industrial Informatics*, *11*(6), 1287−12897. Available from https://doi.org/10.1109/TII.2015.2479856, http://ieeexplore.ieee.org/xpl/RecentIssue.jsp?punumber = 9424.

Hedayatrasa, S., Poelman, G., Segers, J., Van Paepegem, W., & Kersemans, M. (2019). Performance of frequency and/or phase modulated excitation waveforms for optical infrared thermography of CFRPs through thermal wave radar: A simulation study. *Composite Structures*, *225*. Available from https://doi.org/10.1016/j.compstruct.2019.111177.

Hedayatrasa, S., Poelman, G., Segers, J., Van Paepegem, W., & Kersemans, M. (2021). On the application of an optimized frequency-phase modulated waveform for enhanced infrared thermal wave radar imaging of composites. *Optics and Lasers in Engineering*, *138*. Available from https://doi.org/10.1016/j.optlaseng.2020.106411.

Hedayatrasa, S., Poelman, G., Segers, J., Van Paepegem, W., & Kersemans, M. (2022). Phase inversion in (vibro-)thermal wave imaging of materials: Extracting the AC component and filtering nonlinearity. *Structural Control and Health Monitoring*, *29*(4), e2906. Available from https://doi.org/10.1002/stc.2906, https://doi.org/10.1002/stc.2906.

Hedayatrasa, S., Segers, J., Poelman, G., Van Paepegem, W., & Kersemans, M. (2021). Vibro-thermal wave radar: Application of barker coded amplitude modulation for enhanced low-power vibrothermographic inspection of composites. *Materials*, *14*(9). Available from https://doi.org/10.3390/ma14092436, https://www.mdpi.com/1996-1944/14/9/2436/pdf.

Hedayatrasa, S., Segers, J., Poelman, G., Verboven, E., Van Paepegem, W., & Kersemans, M. (2020). Vibrothermographic spectroscopy with thermal latency compensation for effective identification of local defect resonance frequencies of a CFRP with BVID. *NDT & E International*, *109*. Available from https://doi.org/10.1016/j.ndteint.2019.102179.

Hellstein, P., & Szwedo, M. (2016). 3D thermography in non-destructive testing of composite structures. *Measurement Science and Technology*, *27*(12). Available from https://doi.org/10.1088/0957-0233/27/12/124006.

Henneke, E., II, & S.S. Russell, (1983). Impact damage. Detection and evaluation by active and passive thermography and stereo X-ray radiography in advanced composite panels. In: *14th symposium on nondestructive evaluation*.

Henneke, E. G., Reifsnider, K. L., & Stinchcomb, W. W. (1979). Thermography - An NDI method for damage detection. *Journal of Metals*, *31*(9), 11−15.

Herb, V., Martin, E., & Couégnat, G. (2012). Damage analysis of thin 3D-woven SiC/SiC composite under low velocity impact loading. *Composites Part A: Applied Science and Manufacturing*, *43*(2), 247−253. Available from https://doi.org/10.1016/j.compositesa.2011.10.013.

Holland, S. D., Uhl, C., Ouyang, Z., Bantel, T., Li, M., Meeker, W. Q., Lively, J., Brasche, L., & Eisenmann, D. (2011). Quantifying the vibrothermographic effect. *NDT & E International*, *44*(8), 775−782. Available from https://doi.org/10.1016/j.ndteint.2011.07.006.

Ishikawa, M., Hatta, H., Habuka, Y., Fukui, R., & Utsunomiya, S. (2013). Detecting deeper defects using pulse phase thermography. *Infrared Physics and Technology*, *57*, 42−49. Available from https://doi.org/10.1016/j.infrared.2012.11.009.

Karger-Kocsis, J., & Czigány, T. (1998). Effects of interphase on the fracture and failure behavior of knitted fabric reinforced composites produced from commingled GF/PP yarn. *Composites Part A: Applied Science and Manufacturing*, *29*(9−10), 1319−1330. Available from https://doi.org/10.1016/s1359-835x(98)00042-6.

Katunin, A. (2018). A concept of thermographic method for non-destructive testing of polymeric composite structures using self-heating effect. *Sensors (Switzerland)*, *18*(1). Available from https://doi.org/10.3390/s18010074, http://www.mdpi.com/1424-8220/18/1/74/pdf.

Liang, T., Ren, W., Tian, G. Y., Elradi, M., & Gao, Y. (2016). Low energy impact damage detection in CFRP using eddy current pulsed thermography. *Composite Structures*, *143*,

352–361. Available from https://doi.org/10.1016/j.compstruct.2016.02.039, http://www.elsevier.com/inca/publications/store/4/0/5/9/2/8.

Liu, K., Zheng, M., Liu, Y., Yang, J., & Yao, Y. (2023). Deep autoencoder thermography for defect detection of carbon fiber composites. *IEEE Transactions on Industrial Informatics*, *19*(5), 6429–6438. Available from https://doi.org/10.1109/TII.2022.3172902, http://ieeexplore.ieee.org/xpl/RecentIssue.jsp?punumber = 9424.

Maierhofer, C., Myrach, P., Reischel, M., Steinfurth, H., Röllig, M., & Kunert, M. (2014). Characterizing damage in CFRP structures using flash thermography in reflection and transmission configurations. *Composites Part B: Engineering*, *57*, 35–46. Available from https://doi.org/10.1016/j.compositesb.2013.09.036.

Maldague, X. (2001). *Theory and practice of infrared technology for nondestructive testing*. John Wiley & Sons.

Maldague, X., & Marinetti, S. (1996). Pulse phase infrared thermography. *Journal of Applied Physics*, *79*(5), 2694–2698. Available from https://doi.org/10.1063/1.362662.

Mendioroz, A., Celorrio, R., & Salazar, A. (2017). Ultrasound excited thermography: An efficient tool for the characterization of vertical cracks. *Measurement Science and Technology*, *28*(11). Available from https://doi.org/10.1088/1361-6501/aa825a.

Mendioroz, A., Martínez, K., Celorrio, R., & Salazar, A. (2019). Characterizing the shape and heat production of open vertical cracks in burst vibrothermography experiments. *NDT & E International*, *102*, 234–243. Available from https://doi.org/10.1016/j.ndteint.2018.12.006.

Meola, C., & Carlomagno, G. M. (2010). Impact damage in GFRP: New insights with infrared thermography. *Composites Part A: Applied Science and Manufacturing*, *41*(12), 1839–1847. Available from https://doi.org/10.1016/j.compositesa.2010.09.002.

Meola, C., Carlomagno, G. M., Squillace, A., & Vitiello, A. (2006). Non-destructive evaluation of aerospace materials with lock-in thermography. *Engineering Failure Analysis*, *13*(3), 380–388. Available from https://doi.org/10.1016/j.engfailanal.2005.02.007.

Montanini, R., & Freni, F. (2012). Non-destructive evaluation of thick glass fiber-reinforced composites by means of optically excited lock-in thermography. *Composites Part A: Applied Science and Manufacturing*, *43*(11), 2075–2082. Available from https://doi.org/10.1016/j.compositesa.2012.06.004.

Moradi, M., & Safizadeh, M. S. (2019a). Edge disbond detection of carbon/epoxy repair patch on aluminum using thermography. *Composites Science and Technology*, *179*, 41–53. Available from https://doi.org/10.1016/j.compscitech.2019.04.031, https://www.sciencedirect.com/science/article/pii/S0266353819301010.

Moradi, M., & Safizadeh, M. S. (2019b). Experimental and numerical study of the effect of using polyurethane instead of Teflon strip to simulate debonding defect in composite patch repairs aluminum plate under thermography inspection. *Composites Part B: Engineering*, *175*. Available from https://doi.org/10.1016/j.compositesb.2019.107176.

Moradi, M., & Safizadeh, M. S. (2019c). Detection of edge debonding in composite patch using novel post processing method of thermography. *NDT & E International*, *107*. Available from https://doi.org/10.1016/j.ndteint.2019.102153.

Moran, J., & Rajic, N. (2019). Remote line scan thermography for the rapid inspection of composite impact damage. *Composite Structures*, *208*, 442–453. Available from https://doi.org/10.1016/j.compstruct.2018.10.038, http://www.elsevier.com/inca/publications/store/4/0/5/9/2/8.

Patel, P. M., Almond, D. P., & Reiter, H. (1987). Thermal-wave detection and characterisation of sub-surface defects. *Applied Physics B*, *43*(1), 9–15. Available from https://doi.org/10.1007/BF00693966, https://doi.org/10.1007/BF00693966.

Poelman, G., Hedayatrasa, S., Segers, J., Van Paepegem, W., & Kersemans, M. (2020). Adaptive spectral band integration in flash thermography: Enhanced defect detectability and quantification in composites. *Composites Part B: Engineering*, *202*. Available from https://doi.org/10.1016/j.compositesb.2020.108305.

Poelman, G., Hedayatrasa, S., Van Paepegem, W., & Kersemans, M. (2023). Enhanced thermographic inspection of woven fabric composites by k -space filtering. *Composites Part B: Engineering*, *252*. Available from https://doi.org/10.1016/j.compositesb.2023.110508.

Potet, P., Jeannin, P., & Bathias, C. (1987). Use of digital image processing in vibrothermographic detection of impact damage in composite materials. *Materials Evaluation*, *45*(4), 466–470.

Rahammer, M., & Kreutzbruck, M. (2017). Fourier-transform vibrothermography with frequency sweep excitation utilizing local defect resonances. *NDT & E International*, *86*, 83–88. Available from https://doi.org/10.1016/j.ndteint.2016.11.012.

Rajic, N. (2002). Principal component thermography for flaw contrast enhancement and flaw depth characterisation in composite structures. *Composite Structures*, *58*(4), 521–528. Available from https://doi.org/10.1016/S0263-8223(02)00161-7.

Rani, A., Das, P., Sharma, A., Arora, V., Dua, G., & Mulaveesala, R. (2023). Estimation of defect depth in carbon fibre reinforced polymer using frequency modulated thermal wave imaging: An analytical study. *Russian Journal of Nondestructive Testing*, *59*(1), 117–128. Available from https://doi.org/10.1134/S106183092260068X, https://www.springer.com/journal/11181.

Rantala, J., Wu, D., & Busse, G. (1996). Amplitude-modulated lock-in vibrothermography for NDE of polymers and composites. *Research in Nondestructive Evaluation*, *7*(4), 215–228. Available from https://doi.org/10.1007/bf01606389.

Rantala, J., Wu, D., & Busse, G. (1998). NDT of polymer materials using lock-in thermography with water-coupled ultrasonic excitation. *NDT & E International*, *31*(1), 43–49. Available from https://doi.org/10.1016/s0963-8695(97)00021-2.

Renshaw, J., Chen, J. C., Holland, S. D., & Bruce Thompson, R. (2011). The sources of heat generation in vibrothermography. *NDT and E International*, *44*(8), 736–739. Available from https://doi.org/10.1016/j.ndteint.2011.07.012.

Renshaw, J.B. (2009). The mechanics of defect detection in vibrothermography.

Roche, J. M., & Balageas, D. L. (2015). Common tools for quantitative pulse and step-heating thermography - Part II: Experimental investigation. *Quantitative InfraRed Thermography Journal*, *12*(1), 1–23. Available from https://doi.org/10.1080/17686733.2014.996341, http://www.tandfonline.com/toc/tqrt20/currentnalCode = qrt20s.

Ruan, L., Gao, B., Wu, S., & Woo, W. L. (2020). DeftectNet: Joint loss structured deep adversarial network for thermography defect detecting system. *Neurocomputing*, *417*, 441–457. Available from https://doi.org/10.1016/j.neucom.2020.07.093, http://www.elsevier.com/locate/neucom.

Russell, S. S., & Henneke, E. G. (1984). Dynamic effects during vibrothermographic NDE of composites. *NDT International*, *17*(1), 19–25. Available from https://doi.org/10.1016/0308-9126(84)90109-3.

Schroeder, J. A., Ahmed, T., Chaudhry, B., & Shepard, S. (2002). Non-destructive testing of structural composites and adhesively bonded composite joints: Pulsed thermography. *Composites Part A: Applied Science and Manufacturing*, *33*(11), 1511–1517. Available from https://doi.org/10.1016/S1359-835X(02)00139-2.

Segers, J., Hedayatrasa, S., Verboven, E., Poelman, G., Van Paepegem, W., & Kersemans, M. (2019). In-plane local defect resonances for efficient vibrothermography of impacted

carbon fiber-reinforced polymers (CFRP). *NDT & E International*, *102*, 218−225. Available from https://doi.org/10.1016/j.ndteint.2018.12.005.

Shepard, S.M., Lhota, J.R., Rubadeux, B.A., Ahmed, T., & Wang. D. (2002) Enhancement and reconstruction of thermographic NDT data. In *Proceedings of SPIE - The International Society for Optical Engineering* (pp. 531−535) United States, 4710. Available from https://doi.org/10.1117/12.459603.

Shepard, S. M., Lhota, J. R., Rubadeux, B. A., Wang, D., & Ahmed, T. (2003). Reconstruction and enhancement of active thermographic image sequences. *Optical Engineering*, *42*(5), 1337−1342. Available from https://doi.org/10.1117/1.1566969.

Solodov, I., & Busse, G. (2013). Resonance ultrasonic thermography: Highly efficient contact and air-coupled remote modes. *Applied Physics Letters*, *102*(6). Available from https://doi.org/10.1063/1.4792236.

Solodov, I., Derusova, D., & Rahammer, M. (2015a). Thermosonic Chladni figures for defect-selective imaging. *Ultrasonics*, *60*, 1−5. Available from https://doi.org/10.1016/j.ultras.2015.02.007, http://www.elsevier.com/wps/find/journaldescription.cws_home/525452/description#description.

Solodov, I., Rahammer, M., Derusova, D., & Busse, G. (2015b). Highly-efficient and noncontact vibro-thermography via local defect resonance. *Quantitative InfraRed Thermography Journal*, *12*(1), 98−111. Available from https://doi.org/10.1080/17686733.2015.1026018, http://www.tandfonline.com/toc/tqrt20/currentnalCode = qrt20s.

Suzuki, Y., Todoroki, A., Matsuzaki, R., & Mizutani, Y. (2012). Impact-damage visualization in CFRP by resistive heating: Development of a new detection method for indentations caused by impact loads. *Composites Part A: Applied Science and Manufacturing*, *43*(1), 53−64. Available from https://doi.org/10.1016/j.compositesa.2011.09.003.

Tabatabaei, N., & Mandelis, A. (1989). Thermal coherence tomography: Depth-resolved imaging in parabolic diffusion-wave fields using the thermal-wave radar. *International Journal of Thermophysics*, *33*.

Tabatabaei, N., & Mandelis, A. (2011). Thermal coherence tomography using match filter binary phase coded diffusion waves. *Physical Review Letters*, *107*(16). Available from https://doi.org/10.1103/PhysRevLett.107.165901, http://oai.aps.org/filefetch?identifier = 10.1103/PhysRevLett.107.165901&component = fulltext&description = markup&format = xml.

Takeda, S., Aoki, Y., Ishikawa, T., Takeda, N., & Kikukawa, H. (2007). Structural health monitoring of composite wing structure during durability test. *Composite Structures*, *79*(1), 133−139. Available from https://doi.org/10.1016/j.compstruct.2005.11.057.

Tenek, L. H., Henneke, E. G., & Gunzburger, M. D. (1993). Vibration of delaminated composite plates and some applications to non-destructive testing. *Composite Structures*, *23*(3), 253−262. Available from https://doi.org/10.1016/0263-8223(93)90226-G.

Thomas, K. R., & Balasubramaniam, K. (2015). Scanning induction thermography (SIT) for imaging damages in carbon-fibre reinforced plastics (CFRP) components. *AIP Conference Proceedings*, *1650*, 306−313. Available from https://doi.org/10.1063/1.4914624, http://scitation.aip.org/content/aip/proceeding/aipcp.

Truyaert, K., Aleshin, V., Van Den Abeele, K., & Delrue, S. (2019). Theoretical calculation of the instantaneous friction-induced energy losses in arbitrarily excited axisymmetric mechanical contact systems. *International Journal of Solids and Structures*, *158*, 268−276. Available from https://doi.org/10.1016/j.ijsolstr.2018.09.014, journals.elsevier.com/international-journal-of-solids-and-structures/.

Tsoi, K. A., & Rajic, N. (2011). Non-destructive evaluation of aircraft structural components and composite materials at DSTO using sonic thermography. *Defence Science and*

Technology Organisation Victoria (Australia) Air Vehicles Div. Available from https://apps.dtic.mil/sti/citations/tr/ADA540527.

Umar, M. Z., Vavilov, V. P., Abdullah, H., & Ariffin, A. K. (2017). Detecting low-energy impact damages in carbon-carbon composites by ultrasonic infrared thermography. *Russian Journal of Nondestructive Testing*, *53*(7), 530–538. Available from https://doi.org/10.1134/S1061830917070099.

Usamentiaga, R., Venegas, P., Guerediaga, J., Vega, L., & López, I. (2013a). Feature extraction and analysis for automatic characterization of impact damage in carbon fiber composites using active thermography. *NDT & E International*, *54*, 123–132. Available from https://doi.org/10.1016/j.ndteint.2012.12.011.

Usamentiaga, R., Venegas, P., Guerediaga, J., Vega, L., & López, I. (2013b). Automatic detection of impact damage in carbon fiber composites using active thermography. *Infrared Physics & Technology*, *58*, 36–46. Available from https://doi.org/10.1016/j.infrared.2013.01.004.

Usamentiaga, R., Venegas, P., Guerediaga, J., Vega, L., Molleda, J., & Bulnes, F. G. (2014). Infrared thermography for temperature measurement and non-destructive testing. *Sensors (Switzerland)*, *14*(7), 12305–12348. Available from https://doi.org/10.3390/s140712305, http://www.mdpi.com/1424-8220/14/7/12305/pdf.

Vavilov, V., & Burleigh, D. (2020). *Infrared thermography and thermal nondestructive testing infrared thermography and thermal nondestructive testing* (pp. 1–598). Russian Federation: Springer International Publishing. Available from https://link.springer.com/book/10.1007/978-3-030-48002-8, https://doi.org/10.1007/978-3-030-48002-8.

Wong, B. S., Tui, C. G., Bai, W., Tan, P. H., Low, B. S., & Tan, K. S. (1999). Thermographic evaluation of defects in composite materials. *Insight: Non-Destructive Testing and Condition Monitoring*, *41*(8), 504–509.

Yang, R., & He, Y. (2015). Eddy current pulsed phase thermography considering volumetric induction heating for delamination evaluation in carbon fiber reinforced polymers. *Applied Physics Letters*, *106*(23). Available from https://doi.org/10.1063/1.4922524, http://scitation.aip.org/content/aip/journal/apl.

Yang, R., & He, Y. (2016). Polymer-matrix composites carbon fibre characterisation and damage inspection using selectively heating thermography (SeHT) through electromagnetic induction. *Composite Structures*, *140*, 590–601. Available from https://doi.org/10.1016/j.compstruct.2016.01.006, http://www.elsevier.com/inca/publications/store/4/0/5/9/2/8.